

84420
JE

Fibre Optic Sensor for Surface Roughness Measurement

ABSTRACT
by

Jan Bohlmann


Dipl. Ing., Technische Fachhochschule Berlin, 1993


A Thesis Submitted in Partial Fulfillment of the
Requirements for the Degree of

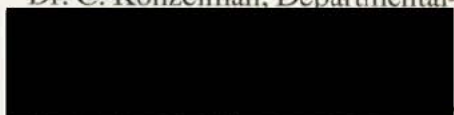
MASTER OF APPLIED SCIENCE

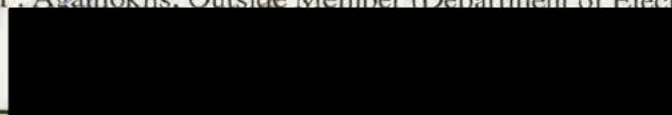
in the Department of Mechanical Engineering


We accept this thesis as conforming
to the required standard

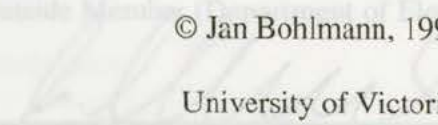

Dr. C. Bradley, Supervisor (Department of Mechanical Engineering)


Dr. C. Konzelman, Departmental Member (Department of Mechanical Engineering)


Dr. P. Agathoklis, Outside Member (Department of Electrical & Computer Engineering)


Dr. R. Vahldieck, External Examiner (Department of Electrical & Computer Engineering)


Dr. P. Agathoklis, Outside Member (Department of Electrical & Computer Engineering)
© Jan Bohlmann, 1995


University of Victoria
Dr. R. Vahldieck, External Examiner (Department of Electrical & Computer Engineering)

All rights reserved. This thesis may not be reproduced in whole or in part, by photocopy or other means, without the permission of the author.

05 110

Supervisor: Dr. C. Bradley

ABSTRACT

The surface roughness of a manufactured part plays an important role in production processes. In some cases the surface roughness needs to meet exact specifications to ensure proper functioning of the part. The key to minimizing production costs is the correct measurement and description of the surface. Two general types of measuring systems are in common use: contact and non-contact devices. A mechanical profiler, for example, works by mechanical contact of a diamond tip that travels over the surface and measures local height variations. In this thesis a fibre optic interferometer sensor system, originally designed to measure pressure variations, is evaluated as a non-contact surface profile measurement device. Software has been developed to calibrate the system and to acquire surface data, which then is used to perform surface parameter calculations. In an evaluating comparison both devices, the stylus and the fibre optic interferometer system, measure the same surface samples which represent different machining processes. Limitations of the system are evaluated by measuring the diameter of the laser spot and its standoff distance from the surface.

Examiners:



Dr. C. Bradley, Supervisor (Department of Mechanical Engineering)



Dr. C. Konzelman, Departmental Member (Department of Mechanical Engineering)



Dr. P. Agathoklis, Outside Member (Department of Electrical & Computer Engineering)



Dr. R. Vahldieck, External Examiner (Department of Electrical & Computer Engineering)

4. SENSOR CALIBRATION THE	Table of Contents	21
4.1. Calibration Against a Michelson Interferometer		21
Abstract		ii
4.2. Laser Spot Size		iii
Using Gaussian Beam Theory		vi
Modeling of Ray Optics		vii
Experiment		ix
4.2.4. Results of Laser Spot Size Calculation		33
1. INTRODUCTION		1
4.3. References		34
1.1. References		3
5. DATA ACQUISITION SOFTWARE		35
2. SURFACE ROUGHNESS MEASUREMENT METHODS		4
5.1. Analog Signal Calibration		35
2.1. Stylus Method		4
5.2. Digital Counter Calibration		37
2.2. Optical Methods		7
5.3. Measuring Surface Profile by Reset Counting		38
2.2.1. Interferometry		7
2.2.2. Triangulation Profile by Interpolation		10
2.3. Conclusion of Surface Parameters		12
2.4. References		13
3. FIBRE OPTIC INTERFEROMETER SENSOR SYSTEM		14
3.1. Method of Operation with Michelson Interferometer		14
3.2. Method of Measurement with Michelson Interferometer		16
6.2.1. Accuracy of Interpolation		51
3.3. System Components		18
6.2.2. Accuracy of Mitutoyo Surface Tester		53
3.4. References		20
6.3. Sensor Operating Specifications		54

4. SENSOR CALIBRATION THEORY	21
4.1. Calibration Against a Michelson Interferometer	21
4.2. Calculation of Laser Spot Size	25
4.2.1. Calculation Using Gaussian Beam Theory	25
4.2.2. Computer Modeling of Ray Optics	30
4.2.3. Knife Edge Experiment	30
4.2.4. Results of Laser Spot Size Calculation	33
4.3. References	34
5. DATA ACQUISITION SOFTWARE	35
5.1. Analog Signal Calibration	35
5.2. Digital Counter Calibration	37
5.3. Measuring Surface Profile by Reset Counting	38
5.4. Measuring Surface Profile by Interpolation	40
5.5. Calculation of Surface Parameters	43
6. SENSOR CALIBRATION MEASUREMENT	46
6.1. Analog Signal Calibration with Michelson Interferometer	46
6.2. Digital Counter Calibration with Michelson Interferometer	48
6.2.1. Accuracy of Interpolation	51
6.2.2. Accuracy of Mitutoyo Surface Tester	53
6.3. Sensor Operating Specifications	54

7. SURFACE TOPOGRAPHY MEASUREMENT	55
7.1. Reset Counting Comparison	55
7.1.1. Measuring Surface Profile by Reset Counting	56
7.1.2. Measuring Surface Profile with Mitutoyo Surface Tester	57
7.1.3. Comparison	59
7.2. Data Interpolation Comparison	59
7.3. Summary of Results	73
7.4. References	80
8. CONCLUSIONS AND FUTURE WORK	81
8.1. Future Work	82
8.1.1. Reducing Laser Spot Size	82
8.1.2. Autofocus Method	83
8.1.3. Increasing the Power of the Laser Diode	85
8.2. References	86
9. APPENDIX A	87
10. APPENDIX B	94

List of Tables

TABLE 2.1 COMPARISON OF STYLUS AND OPTICAL METHODS	12
TABLE 4.1: FIBRE PROPERTIES	25
TABLE 4.2: PROPERTIES FOR GRIN LENS	28
TABLE 4.3: MEASUREMENT OF SPOT SIZE	32
TABLE 4.4: RESULTS OF LASER SPOT SIZE	33
TABLE 6.1: CONTROLS DIGITAL COUNTER CALIBRATION	49
TABLE 6.2: MEASURED VOLTAGES FOR INTERPOLATION MEASUREMENT	53
TABLE 7.1: CONTROLS RESET COUNTING	56
TABLE 7.2: CONTROLS MITUTOYO SURFACE TESTER	58
TABLE 7.3: CONTROLS MEASURING SURFACE PROFILE BY INTERPOLATION	61
TABLE 7.4: COMPARISON OF MEASURED DATA	74
FIGURE 3.1: CALIBRATION ARRANGEMENT	21
FIGURE 4.2: TWO COHERENT LIGHT WAVES	22
FIGURE 4.3: POISS OUTPUT	23
FIGURE 4.4: GRIN LENS	26
FIGURE 4.5: KNIFE EDGE EXPERIMENT	31
FIGURE 4.6: LASER SPOT SIZE CHARACTERISTICS	32
FIGURE 5.1: FLOWCHART, ANALOG SIGNAL CALIBRATION	36
FIGURE 5.2: FLOWCHART, DIGITAL COUNTER CALIBRATION	37
FIGURE 5.3: FLOWCHART, MEASURING SURFACE PROFILE BY COUNTING RESETS	39
FIGURE 5.4: FLOWCHART, MEASURING SURFACE PROFILE BY INTERPOLATION	42
FIGURE 5.5: FLOWCHART, MITUTOYO SURFACE TESTER	44
FIGURE 6.1: ANALOG SIGNAL CALIBRATION TOWARDS	47
FIGURE 6.2: ANALOG SIGNAL CALIBRATION AWAY	48
FIGURE 6.3: DIGITAL COUNTER CALIBRATION TOWARDS	50
FIGURE 6.4: DIGITAL COUNTER CALIBRATION AWAY	51
FIGURE 6.5: FRINGE MOVEMENT FOR INTERPOLATION MEASUREMENT	52
FIGURE 6.6: ACCURACY OF THE MITUTOYO SURFACE TESTER	54
FIGURE 7.1: FRONT PANEL RESET COUNTING	57
FIGURE 7.2: FRONT PANEL MITUTOYO SURFACE TESTER	58
FIGURE 7.3: POISS MEASUREMENT, SAMPLE #1	63
FIGURE 7.4: MITUTOYO MEASUREMENT, SAMPLE #1	64
FIGURE 7.5: POISS MEASUREMENT, SAMPLE #2	66

List of Figures

FIGURE 2.0: MITUTOYO MEASUREMENT, SAMPLE #0	67
FIGURE 2.1: SCHEMATIC VIEW OF PROFILOMETER	5
FIGURE 2.2: ILLUSTRATION OF A PROFILE	5
FIGURE 2.3: SURFACE SCRATCHED BY STYLUS	6
FIGURE 2.4: INTERFERENCE FRINGE PATTERN.	8
FIGURE 2.5: PHASE DIFFERENCE	9
FIGURE 2.6: INTERFEROMETER FOR TESTING SURFACES (MI)	10
FIGURE 2.7: (A) PHYSICAL LAYOUT AND (B) GEOMETRICAL LAYOUT	11
FIGURE 3.1: FIBRE OPTIC INTERFEROMETER SENSOR SYSTEM DESIGN	14
FIGURE 3.2: OPERATION OF GRIN LENS	15
FIGURE 3.3: RESET AND PRESET OF FOISS	17
FIGURE 3.4: SENSOR TRANSLATION STAGE.	18
FIGURE 4.1: CALIBRATION ARRANGEMENT	21
FIGURE 4.2: TWO COHERENT LIGHT WAVES	22
FIGURE 4.3: FOISS OUTPUT	23
FIGURE 4.4: GRIN LENS	26
FIGURE 4.5: KNIFE EDGE EXPERIMENT	31
FIGURE 4.6: LASER SPOT SIZE CHARACTERISTICS	32
FIGURE 5.1: FLOWCHART, ANALOG SIGNAL CALIBRATION	36
FIGURE 5.2: FLOWCHART, DIGITAL COUNTER CALIBRATION	37
FIGURE 5.3: FLOWCHART, MEASURING SURFACE PROFILE BY COUNTING RESETS	39
FIGURE 5.4: FLOWCHART, MEASURING SURFACE PROFILE BY INTERPOLATION	42
FIGURE 5.5: FLOWCHART, MITUTOYO SURFACE TESTER	44
FIGURE 6.1: ANALOG SIGNAL CALIBRATION TOWARDS	47
FIGURE 6.2: ANALOG SIGNAL CALIBRATION AWAY	48
FIGURE 6.3: DIGITAL COUNTER CALIBRATION TOWARDS	50
FIGURE 6.4: DIGITAL COUNTER CALIBRATION AWAY	51
FIGURE 6.5: FRINGE MOVEMENT FOR INTERPOLATION MEASUREMENT	52
FIGURE 6.6: ACCURACY OF THE MITUTOYO SURFACE TESTER	54
FIGURE 7.1: FRONT PANEL RESET COUNTING	57
FIGURE 7.2: FRONT PANEL MITUTOYO SURFACE TESTER	58
FIGURE 7.3: FOISS MEASUREMENT, SAMPLE #1	63
FIGURE 7.4: MITUTOYO MEASUREMENT, SAMPLE #1	64
FIGURE 7.5: FOISS MEASUREMENT, SAMPLE #2	66

FIGURE 7.6: MITUTOYO MEASUREMENT, SAMPLE #2	67
FIGURE 7.7: FOISS MEASUREMENT, SAMPLE #3	68
FIGURE 7.8: MITUTOYO MEASUREMENT, SAMPLE #3	69
FIGURE 7.9: FOISS MEASUREMENT, SAMPLE #4	71
FIGURE 7.10: MITUTOYO MEASUREMENT, SAMPLE #4	72
FIGURE 7.11: CALIBRATION ERROR	76
FIGURE 7.12: SPOT SIZE IN COMPARISON TO SURFACE	78
FIGURE 8.1: LASER SPOT SIZE CHARACTERISTICS	83
FIGURE 8.2: AUTOFOCUS METHOD	84
FIGURE 8.3: SPOT SIZE LIMITATION	84
FIGURE 9.1: TYPICAL SURFACE LAYERS	87
FIGURE 9.2: THE CONSTITUENT GEOMETRIC COMPONENTS OF A SOLID SURFACE	88
FIGURE 9.3: SCHEMATIC SURFACE PROFILE $Y(X)$	89
FIGURE 9.4: GEOMETRIC PROFILES HAVING THE SAME RA VALUES	90
FIGURE 9.5: EXAMPLE OF SINUSOIDAL SURFACE	92
FIGURE 10.1: SCHEMATIC FOR DIGITAL CARD	94

Glossary of Abbreviations

For the reader's convenience the following abbreviations will be used throughout this manuscript:

Fibre optic interferometer sensor system	FOISS
Gradient Index	GRIN
Michelson Interferometer	MI
Data acquisition	DAQ
Virtual instruments	VI

- 1) Fatigue Life: components under stress reversals tend to fail at surface irregularities.
- 2) Wear: components with high surface peaks will wear faster than those with a smooth surface, due to scoring.
- 3) Friction: components with a smooth surface have a lower friction factor, which saves energy when two parts of the same material are sliding on each other.

These examples illustrate that the roughness of a surface is quite significant and that during the design of a component, surface roughness has to be considered at all times. Both designer and process planner must have a very good understanding of surface roughness and its implications [4], and they need to be able to determine the roughness of a part at any time during the manufacturing process.

Viewed under a microscope, surfaces have a great number of peaks and quantifying them all would be an overwhelming task. Therefore, measurements of roughness are typically made on a small but representative sample of the surface. Industry uses many different methods to measure surface roughness. Generally, surface roughness is monitored by randomly recording a surface profile along a line on the

1. Introduction

An extremely rough bore can stop a rotating shaft cold. Using a finer finish at first solves the problem, but after run-in time the shaft once again seizes up. Surfaces are now too smooth, allowing no room for lubricants. The required surface texture depends on the part's final function. Will it seal, slide, reciprocate, or simply look smooth? Will it move fast or slow? Is noise a concern? Is painting or plating necessary? How long must the part last without repair?

In the past, a machinist might have used his fingernail for a qualitative evaluation of surface condition in manual operation [1], but today's manufacturing world requires more sensitive sensors. Knowledge of the roughness of a surface can help to determine when a part will break down. It will also give information in the following areas [2, 3].

- 1) Fatigue Life: components under stress reversals tend to fail at surface irregularities.
- 2) Wear: components with high surface peaks will wear faster than those with a smooth surface, due to scoring.
- 3) Friction: components with a smooth surface have a lower friction factor, which saves energy when two parts of the same material are sliding on each other.

These examples illustrate that the roughness of a surface is quite significant and that during the design of a component, surface roughness has to be considered at all times. Both designer and process planner must have a very good understanding of surface roughness and its implications [4], and they need to be able to determine the roughness of a part at any time during the manufacturing process.

Viewed under a microscope, surfaces have a great number of peaks and quantifying them all would be an overwhelming task. Therefore, measurements of roughness are typically made on a small but representative sample of the surface. Industry uses many different methods to measure surface roughness. Generally, surface roughness is monitored by randomly recording a surface profile along a line on the

sample and calculating the surface statistics from such a record. However, over the years, quality standards have been raised and are now so high that often a single sample is not enough and the whole surface has to be inspected. Using old inspection techniques, the entire production line would have to be shut down for the roughness evaluation process. Clearly this is impractical, so to save time and money, a non-contact and on-line system is needed -- providing smoother surfaces with less surface damage. Fabrication shops can then have instruments for process control during manufacturing [5].

The objective of this thesis is to analyze and discuss whether a fibre optic interferometer sensor system (FOISS), designed and manufactured for pressure measurement by Canadian Instrumentation and Research (Burlington, Ontario) can be used for non-contact surface roughness measurement. First, an overview of today's different surface measuring principles presents a clear context for this study. Following that, the FOISS operation principle is examined in more detail. The theory for both the calibration and the developed software provides the background for the actual sensor calibration measurement. To evaluate the system's performance as a surface roughness measuring device four different sample surfaces are measured and compared to the data acquired by a stylus measurement, as the stylus is widely used in today's industry. Finally, results and suggestions for future work are summarized in a conclusion. The Appendix provides an overview of surface geometry, characterization and different surface parameters.

1.1. References Surface Measurement Methods

The industrial requirements for accurate characterization of surface roughness

[1] Schaffer, G. H., "The Many Faces of Surface Texture," *American Machinist & Automated Manufacturing*, June 1988: 61-68.

implemented in industry. These technological methods can be divided into two groups:

[2] Whitehouse, D.J., "Typology of Manufactured Surfaces," *Annals of the C.I.R.P.*, vol. XXIV, 1971: 417-431.

[3] De Bruin, W., "Surface and Function," *Annals of the C.I.R.P.*, vol. 35, no. 2, 1986: 551-562.

2.1. Stylus Method

[4] Noaker, Paula M. (ed.) "Scrutinizing Surface Measurement" *Manufacturing Engineering*, vol. 4, 1991: 47.

[5] Bennett, Jean M. *Surface Measurement and Characterization*. The International Society for Optical Engineering: Paper 1009-01, 1989.

traversal of the stylus can be done either manually or mechanically. The traversal of a mechanical power drive results in constant speed of travel of the stylus and thus produces more consistent readings.

As the stylus traverses the surface, the roughness causes a vertical movement which is transmitted to a coil inside the tracer body. The coil moves in the field of a permanent magnet which produces a small fluctuating voltage whose amplitude is directly proportional to the height of the surface profile.

Figure 2.1 Illustration of a profile

2. Surface Roughness Measurement Methods

The industrial requirements for accurate characterization of surface roughness have resulted in the development of different measuring instruments that can be implemented in industry. These technological methods can be divided into two groups: i) Stylus method (contact with surface) and ii) optical method (non-contact). This chapter will describe and compare these two techniques.

2.1. Stylus Method

The most widely accepted instrument for surface roughness measurement is the stylus profilometer. This device consists of a very fine diamond stylus, with a tip radius of typically $12.5\ \mu\text{m}$, which is drawn across the surface as shown in Figure 2.1. The traversal of the stylus can be done either manually or mechanically. The traversal of a mechanical power drive results in constant speed of travel of the stylus and thus produces more consistent readings.

As the stylus traverses the surface, the roughness causes a vertical movement which is transmitted to a coil inside the tracer body. The coil moves in the field of a permanent magnet which produces a small fluctuating voltage whose amplitude is directly proportional to the height of the surface profile.



Figure 2.2: Illustration of a profile

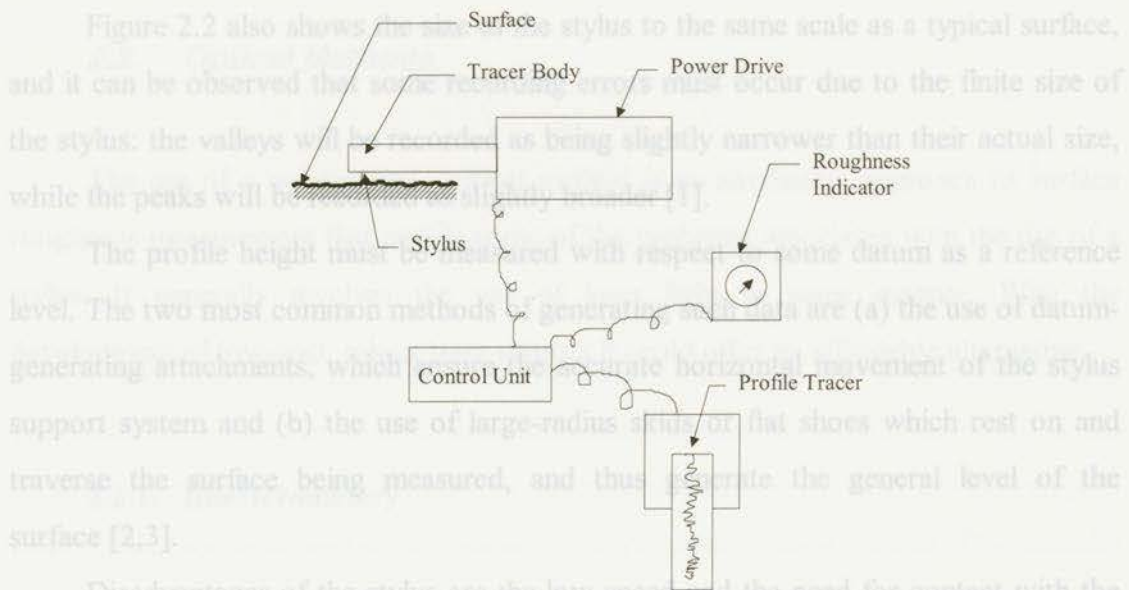


Figure 2.1: Schematic view of profilometer

The vertical magnification is controlled electronically and can normally be varied from $\times 500$ to $\times 100,000$, according to the resolution required. The horizontal magnification is the ratio between the speed of the recording paper and the traverse speed of the stylus, and is typically $\times 100$. This difference between the two magnifications is useful as it gives greater emphasis to the important height characteristics of the surface, but it can lead to a misinterpretation of the results. For example in Figure 2.2 (a) a typical record together with (b) a record using different magnifications. The former record (a) shows that the asperities are undulations with slopes of a few degrees rather than the sharp peaks as could be interpreted from the distorted profile (b).

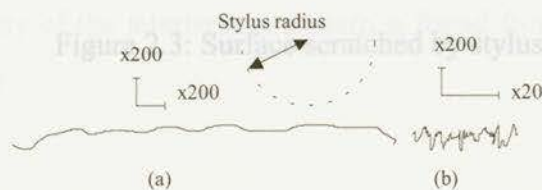


Figure 2.2: Illustration of a profile

Figure 2.2 also shows the size of the stylus to the same scale as a typical surface, and it can be observed that some recording errors must occur due to the finite size of the stylus: the valleys will be recorded as being slightly narrower than their actual size, while the peaks will be recorded as slightly broader [1].

The profile height must be measured with respect to some datum as a reference level. The two most common methods of generating such data are (a) the use of datum-generating attachments, which ensure the accurate horizontal movement of the stylus support system and (b) the use of large-radius skids or flat shoes which rest on and traverse the surface being measured, and thus generate the general level of the surface [2,3].

Disadvantages of the stylus are the low speed and the need for contact with the inspected surface. The marks that a stylus leaves behind can be seen in Figure 2.3. Another disadvantage is generated through manual calibration. The stylus is calibrated by manually adjusting the instrument gain during the traversal over a specimen of known Ra . Although a stylus instrument is adequate for laboratory inspection of surface samples, it is certainly not applicable for on-line inspection, it is not precise, unsuitable for on-line inspection and does not generate a surface profile.



Figure 2.3: Surface scratched by stylus

2.2. Optical Methods

$$I = |A_1 + A_2|^2 = (A_1 + A_2)(A_1^* + A_2^*) \quad (2.3)$$

The use of a non-contact, optical method is an alternative approach to surface roughness measurement that avoids some of the problems associated with the use of a stylus. It generally involves the use of laser light in some manner. With the development of low-cost, robust laser sources it could offer an affordable alternative.

A_1 and A_2 are the amplitudes of the individual waves and $\Delta\phi = \phi_1 - \phi_2$ is the relative phase difference. It is the relative phase difference between the waves that results in the fringe pattern. Interference is typically created by forming an optical path length difference between the two waves or "arms" of the interferometer. The intensity of the interference pattern is given by

2.2.1. Interferometry

Optical interferometers have been used for the inspection of smooth surfaces, particularly for optical components such as mirrors and reflectors. Interferometers function on the principle of interference between two coherent light waves, which results when the waves combine either constructively or destructively, as demonstrated in Young's double slit experiment [4]. Interference results in a redistribution of light intensity in a ring pattern. Constructive interference results in a bright fringe whereas destructive interference results in a dark fringe.

In mathematical terms, interference can be described as follows. Consider two harmonic light waves represented using the complex notation

$$A_1 = a_1 \exp(-i\phi_1) \quad (2.1)$$

$$A_2 = a_2 \exp(-i\phi_2) \quad (2.2)$$

where ϕ_1 and ϕ_2 are the phases of the respective waves and a_1 and a_2 are the amplitudes. The intensity of the interference pattern is found from the combination of the complex amplitudes

$$I = |A_1 + A_2|^2 = (A_1 + A_2)(A_1^* + A_2^*) \quad (2.3)$$

$$= |A_1|^2 + |A_2|^2 + A_1 A_2^* + A_1^* A_2 \quad (2.4)$$

$$= I_1 + I_2 + 2(I_1 I_2)^{1/2} \cos(\Delta\phi) \quad (2.5)$$

I_1 and I_2 are the intensities of the individual waves and $\Delta\phi = \phi_1 - \phi_2$ is the relative phase difference. It is the relative phase difference between the waves that results in the fringe pattern. The phase difference is typically created by forming an optical path length difference between the two waves or "arms" of the interferometer. The intensity or fringe pattern corresponding to (2.5) has the form shown below in Figure 2.4.

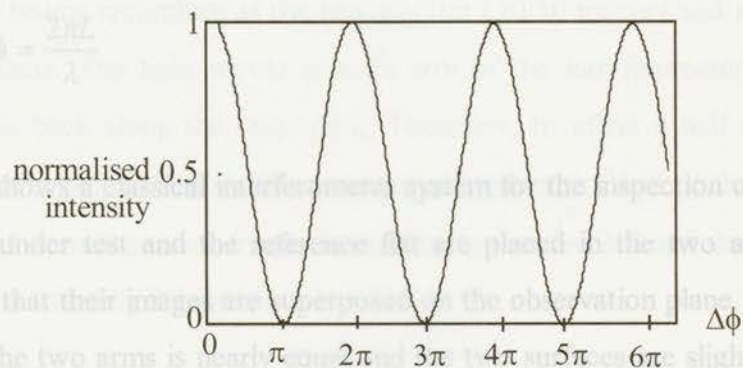


Figure 2.4: Interference fringe pattern.

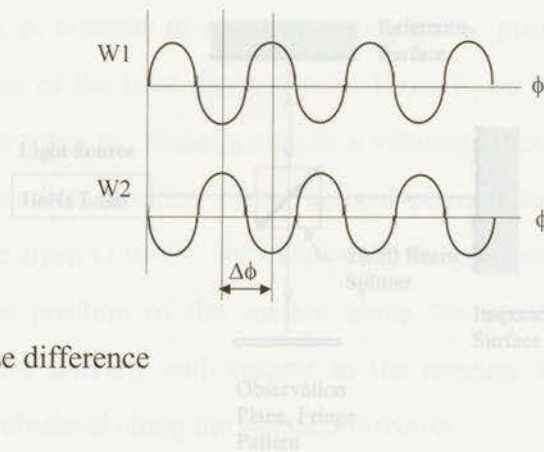


Figure 2.5: Phase difference

Figure 2.5 shows the phase difference between the two waves that are created by forming a physical path length difference (L) from a lens to the surface of the specimen under examination. The relationship between phase, wavelength and path length difference is

$$\Delta\phi = \frac{2\pi L}{\lambda} \quad (2.6)$$

Figure 2.6 shows a classical interferometer system for the inspection of a surface [5]. The surface under test and the reference flat are placed in the two arms of the interferometer so that their images are superposed on the observation plane. If the path difference along the two arms is nearly equal and the two surfaces are slightly tilted, a set of parallel fringes can be observed. Deformation of the fringe pattern can be related to the surface microstructure.

2.2.2. Triangulation

The second optical method is the common geometrical optics profilometer a method which has been well established practice in land surveillance and navigation based on triangulation [6]. This section will describe the basic principle of this method.

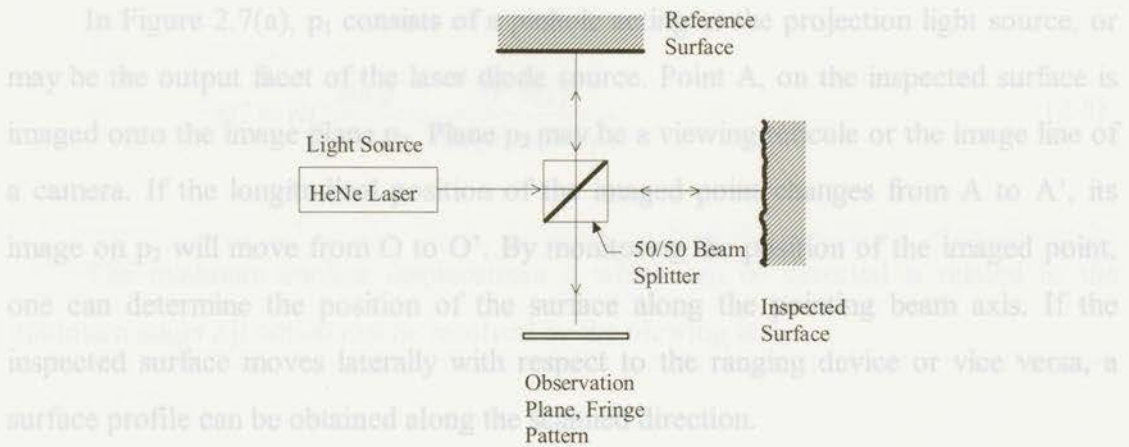


Figure 2.6: Interferometer for testing surfaces (MI)

The path difference changes when the distance to the inspected surface increases or decreases. The beams recombine at the beamsplitter (50/50 mirror) and interfere on the observation plane. The light waves in each arm of the interferometer strike the surface and double back along the same path. Therefore, to effect a half-wavelength ($\lambda/2$) path difference, only a height difference (or movement) of $\lambda/4$ of the inspected surface is needed. For each passing fringe the surface has moved $\lambda/2$ and the distance d can be measured by counting fringes m .

$$d = \frac{m \cdot \lambda}{2} \tag{2.7}$$

2.2.2. Triangulation

The second optical method is the common geometrical optics profilometer a method which has been well established practice in land surveillance and navigation based on triangulation [6]. This section will describe the basic principle of this method.

The optical geometry of the triangulation system is shown in Figure 2.7 (b), where B and C are the object model points of the two lens systems. The distance D between B and C is a known parameter, as is the angle γ . For a given surface position the angle β is measured. The range AC can thus be obtained from the law of sines

In Figure 2.7(a), p_1 consists of a pinhole acting as the projection light source, or may be the output facet of the laser diode source. Point A, on the inspected surface is imaged onto the image plane p_2 . Plane p_2 may be a viewing reticule or the image line of a camera. If the longitudinal position of the imaged point changes from A to A', its image on p_2 will move from O to O'. By monitoring the position of the imaged point, one can determine the position of the surface along the pointing beam axis. If the inspected surface moves laterally with respect to the ranging device or vice versa, a surface profile can be obtained along the scanned direction.

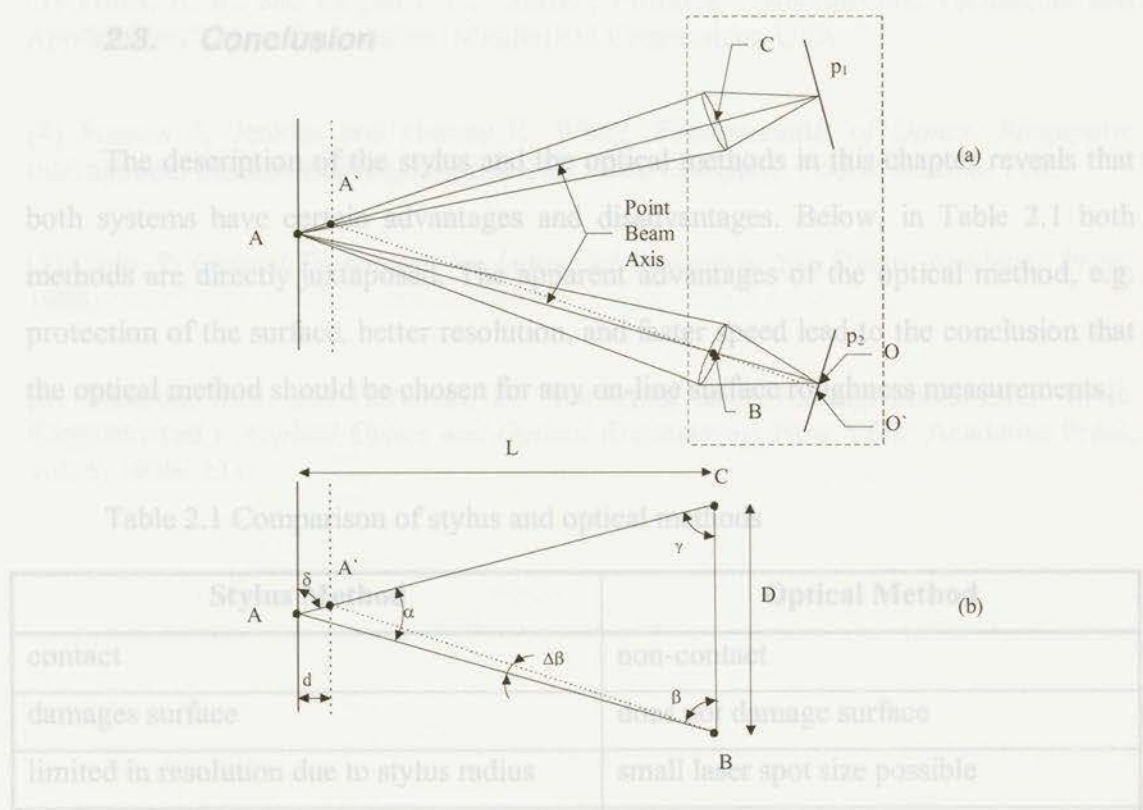


Figure 2.7: (a) Physical layout and (b) geometrical layout

The optical geometry of the triangulation system is shown in Figure 2.7 (b), where B and C are the object model points of the two lens systems. The distance D between B and C is a known parameter, as is the angle γ . For a given surface position the angle β is measured. The range AC can thus be obtained from the law of sines

2.4. References

$$AC = BC \frac{\sin \beta}{\sin \alpha} = \frac{D \cdot \sin \beta}{\sin(\pi - \beta - \gamma)} \quad (2.8)$$

[1] Noaker, Paula M. (ed.) "How Smooth is Smooth Enough?" *Manufacturing Engineering*. The minimum surface displacement d which can be detected is related to the minimum angle $\Delta\beta$ which can be resolved by the viewing lens.

[2] Arnell, R.D. *Tribology: Principles and Design Applications*. New York: Springer Verlag, 1991.

[3] Triax, B. E., and Biegen J. F., "Surface Profiling -- Instruments, Techniques and Applications", Middlefield Connecticut, USA.

2.3. Conclusion

[4] Francis A. Jenkins and Harvey E. White, *Fundamentals of Optics*. Singapore: International Science Publishers, 1977.

The description of the stylus and the optical methods in this chapter reveals that both systems have certain advantages and disadvantages. Below, in Table 2.1 both methods are directly juxtaposed. The apparent advantages of the optical method, e.g. protection of the surface, better resolution, and faster speed lead to the conclusion that the optical method should be chosen for any on-line surface roughness measurements.

[5] Kingslake (ed.), *Applied Optics and Optical Engineering*. New York: Academic Press, vol. 5, 1969: 231.

Table 2.1 Comparison of stylus and optical methods

Stylus Method	Optical Method
contact	non-contact
damages surface	does not damage surface
limited in resolution due to stylus radius	small laser spot size possible
low speed of stylus	fast traverse of laser spot
good for laboratory inspection	on-line measurement possible
resolution 0.1 μm	resolution 0.01 μm
accuracy $\pm 8\%$	accuracy $\pm 2\%$
direct contact with surface	standoff distance 1 mm to 10 mm

2.4. References

3. Fibre Optic Interferometer Sensor System

[1] Noaker, Paula M. (ed.) "How Smooth is Smooth Enough?" *Manufacturing Engineering*, vol. 4, 1993: 47.

[2] Arnell, R.D. *Tribology, Principles and Design Applications*. New York: Springer Verlag, 1991.

[3] Truax, B. E., and Biegen J. F., "Surface Profiling -- Instruments, Techniques and Applications" Zygo Corporation, Middlefield Connecticut, USA.

[4] Francis A. Jenkins and Harvey E. White. *Fundamentals of Optics*. Singapore: International Student Edition, Mcgraw-Hill Book Company, Fourth Edition, 1985.

[5] Cielo, P. *Optical Techniques for Industrial Inspection*. San Diego: Academic Press, 1988.

[6] Dickson, M.S. and Harkness, D. "Surveying and Tracking Instruments" in R. Kingslake (ed.). *Applied Optics and Optical Engineering*, New York: Academic Press, vol. 5, 1969: 231.



Figure 3.1: Fibre Optic Interferometer Sensor System design

3. Fibre Optic Interferometer Sensor System

The shortcomings of the stylus profilometer create a need for improved optical techniques. Based on the principle of interferometry, CIR designed and manufactured a fibre optic interferometer sensor system (FOISS). The FOISS is intended to be used as a fibre optic pressure sensor (measures deflection of a diaphragm).

The principle of operation and the experimental system components of the FOISS will be discussed in this chapter.

3.1. Method of Operation

The FOISS, as illustrated in Figure 3.1, is described below.

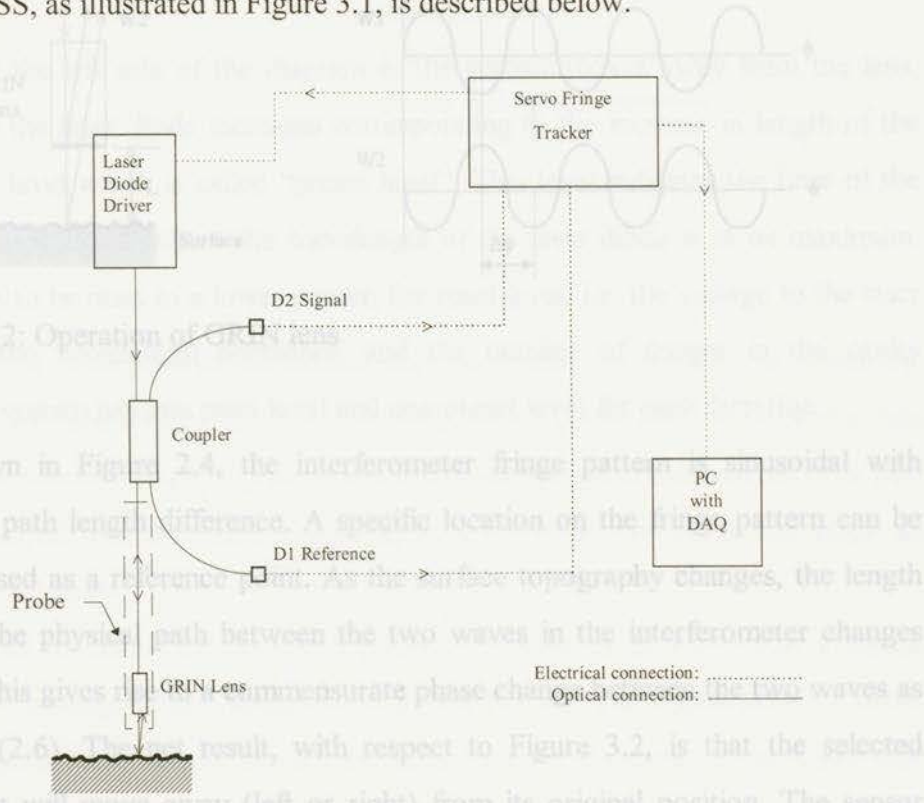


Figure 3.1: Fibre Optic Interferometer Sensor System design

The system uses a laser diode with an output power of 10 mW and an operating wavelength of 787 nm, pigtailed to the coupler. The laser wavelength can be modulated by altering the drive current to the diode. This also affects the relative phase difference as specified by equation (2.6). The laser light is launched into the fibre and is then split into the probe and reference signals by a 50:50 fibre coupler. A detector, D1, monitors the reference signal from one port of the coupler. The other port is connected to a GRIN lens which acts as the probe head.

The target surface reflects light back into the GRIN lens where it is re-captured as illustrated in Figure 3.2. Optical interference occurs between the reflected target light, W2, and the Fresnel reflection [1] from the surface of the GRIN lens, W1. The resulting interference distribution is guided back along the fibre through the coupler where it is detected on photodiode D2.

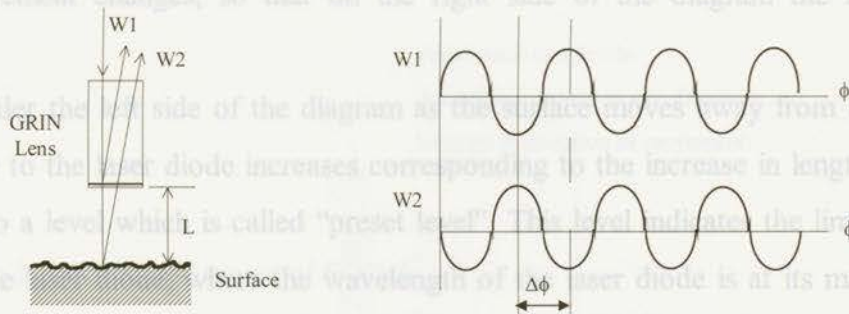


Figure 3.2: Operation of GRIN lens

As shown in Figure 2.4, the interferometer fringe pattern is sinusoidal with respect to the path length difference. A specific location on the fringe pattern can be selected and used as a reference point. As the surface topography changes, the length difference of the physical path between the two waves in the interferometer changes accordingly. This gives rise to a commensurate phase change between the two waves as expressed by (2.6). The net result, with respect to Figure 3.2, is that the selected reference point will move away (left or right) from its original position. The sensor electronics monitor the degree of movement created by this relative phase change and

compensate for the change by altering the drive voltage to the laser diode, and hence altering the wavelength to keep the same number of fringes in the cavity. Therefore, the laser diode drive voltage is used as a metric for the surface topography variation. When the upper or lower limit of the drive current to the laser diode is reached, the system needs to “reset”, as explained in the following section.

3.2. Method of Measurement

Figure 3.3 illustrates the laser diode driver voltage output of the FOISS, as the physical distance between the surface and the GRIN lens - the cavity length - is varied. On the left side of the diagram the cavity length is increasing. At point d, the direction of the movement changes, so that on the right side of the diagram the cavity is decreasing.

Consider the left side of the diagram as the surface moves away from the lens. The voltage to the laser diode increases corresponding to the increase in length of the cavity, up to a level which is called “preset level”. This level indicates the limit of the power to the laser diode, where the wavelength of the laser diode is at its maximum. The FOISS has to be reset to a lower power, the reset level, i.e. the voltage to the laser diode drops, the wavelength decreases, and the number of fringes in the cavity increases. The system has one reset level and one preset level for each direction.

Thus, the presets and resets shown are not consistent. The real levels are measured with an oscilloscope and their values are shown in the graph as horizontal, dashed lines.

To be able to detect the reset and preset and count them accurately, a digital counter card was designed and implemented in the FOISS. The digital counter either increases or decreases if a reset occurs, depending on the direction of the reset. The schematic for the digital card is shown in Appendix B.

3.3. System Components

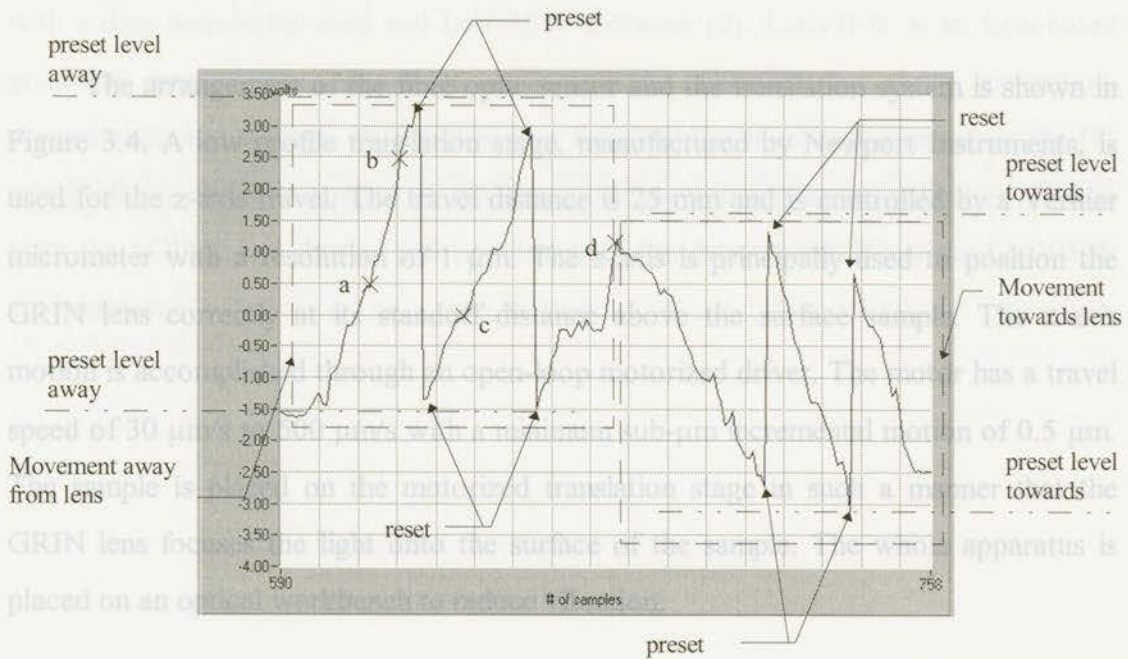


Figure 3.3: Reset and preset of FOISS

Later in the work it was discovered that the output of the FOISS integrator during a reset changes so quickly that the DAQ board is not able to track the real preset and reset levels. Thus, the presets and resets shown are not consistent. The real levels are measured with an oscilloscope and their values are shown in the graph as horizontal, dashed lines.

To be able to detect the reset and preset and count them accurately, a digital counter card was designed and implemented in the FOISS. The digital counter either increases or decreases if a reset occurs, depending on the direction of the reset. The schematic for the digital card is shown in Appendix B.

3.3. System Components

The arrangement of the fibre optic sensor and the translation system is shown in Figure 3.4. A low profile translation stage, manufactured by Newport Instruments, is used for the z-axis travel. The travel distance is 25 mm and is controlled by a Vernier micrometer with a resolution of 1 μm . The z-axis is principally used to position the GRIN lens correctly at its standoff distance above the surface sample. The x-axis motion is accomplished through an open-loop motorized driver. The motor has a travel speed of 30 $\mu\text{m/s}$ to 500 $\mu\text{m/s}$ with a minimum sub- μm incremental motion of 0.5 μm . The sample is placed on the motorized translation stage in such a manner that the GRIN lens focuses the light onto the surface of the sample. The whole apparatus is placed on an optical workbench to reduce vibration.

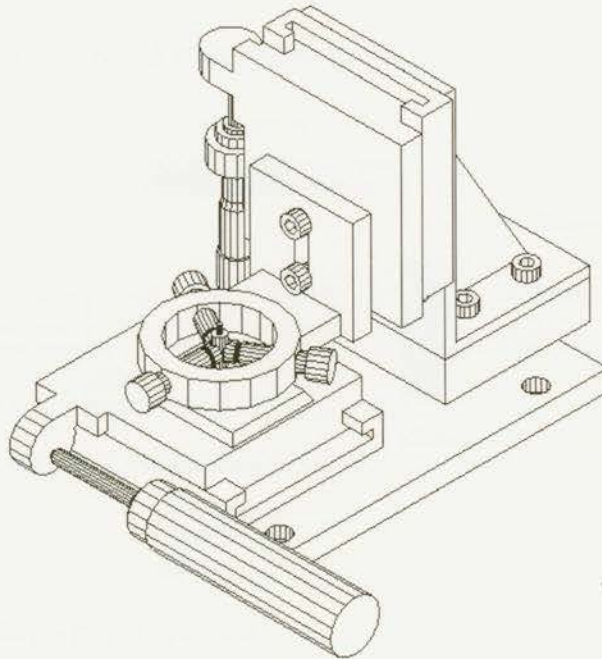


Figure 3.4: Sensor translation stage.

Overall control of the sensor is provided by a 486 DX/2 33MHz PC equipped with a data acquisition card and LabVIEW software [2]. LabVIEW is an icon-based graphical programming language with specific libraries for data acquisition, presentation, and storage. A graphical user interface has been implemented on the PC which allows the user control of the motor and positioning stage, collection of data from the FOISS, and display and processing of the data on the PC in the LabVIEW environment.

for Windows, User Manual, National Instruments Corporation, December 1993.

4.1 Calibration Against a Reference Interferometer

The calibration is performed with a separate MIOT instrument as shown in Figure 4.1.



Figure 4.1 Calibration Arrangement

The MIOT sensor is a Michelson interferometer with a mirror length of 6.125 mm, which is split into two paths of 3.0625 mm each. After each path is reflected

3.4. References

[1] Francis A. Jenkins and Harvey E. White, *Fundamentals of Optics*. Singapore: International Student Edition, McGraw-Hill Book Company, Fourth Edition, 1985.

[2] *LabVIEW for Windows, User Manual*. National Instruments Corporation, December 1993.

Before accurate measurements can be conducted, the FOISS has to be calibrated. This chapter explains both the calibration process using a Michelson Interferometer (MI) and methods for determining the spot size.

4.1. Calibration Against a Michelson Interferometer

The calibration is performed with a separate MI as illustrated in Figure 4.1.

The calibration is performed with a separate MI as illustrated in Figure 4.1. A HeNe laser beam is directed into the interferometer. The distance that the mirror moves is known, the fringe displacement that occurs while the mirror is moving is known, and the fringe displacement that occurs while the mirror is moving is known.



Figure 4.1: Calibration arrangement

The MI consists of a beam of light from a HeNe laser with a wavelength of 632.8 nm, which is split into two beams by a 50:50 beamsplitter. After each beam is reflected

4. Sensor Calibration Theory

Before accurate measurements can be conducted, the FOISS has to be calibrated and its resolution needs to be determined. In order to calculate surface roughness, the relationship between the voltage change and the physical distance change has to be determined. The most accurate calibration method is to use a second interferometer system. Additionally, the spot size of the laser has to be known, since it affects the resolution of the FOISS. This chapter explains both the calibration process using a Michelson Interferometer (MI) and methods for determining the spot size.

4.1. Calibration Against a Michelson Interferometer

The calibration is performed with a separate MI as illustrated in Figure 4.1.

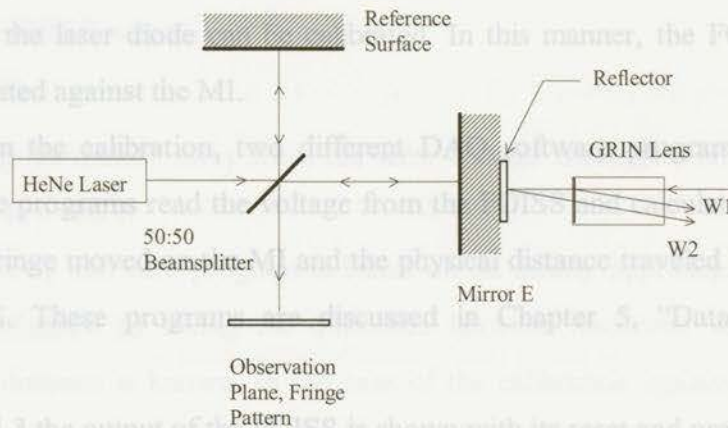


Figure 4.1: Calibration arrangement

The MI consists of a beam of light from a HeNe laser with a wavelength of 632.8 nm, which is split into two beams by a 50:50 beamsplitter. After each beam is reflected

from the reference surface and mirror E, they are recombined at the beamsplitter and an interference fringe pattern can be displayed on the observation plane. In Figure 4.2, the path difference of two coherent light waves is illustrated. In this case, they cancel each other out and a dark fringe appears on the observation plane. If the mirror (E) moves back or forth, concentric fringes appear and disappear at the observation plane. The movement of the mirror can be determined accurately by counting the fringes.

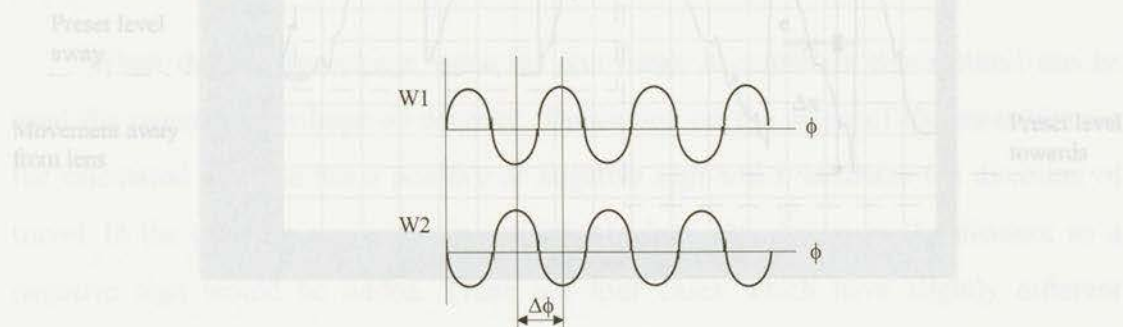


Figure 4.2: Two coherent light waves

A reflector is glued on the back side of the moving mirror (E) and the GRIN lens is focused onto the reflector. Since the distance that the mirror moves is known, the drive voltage of the laser diode can be calibrated. In this manner, the FOISS can be accurately calibrated against the MI.

To perform the calibration, two different DAQ software programs have been developed. These programs read the voltage from the FOISS and calculate the voltage change for one fringe moved on the MI and the physical distance traveled for one reset from the FOISS. These programs are discussed in Chapter 5, "Data Acquisition Software".

In Figure 4.3 the output of the FOISS is shown with its reset and preset levels.

$$b - a \approx \text{one fringe} \quad (4.1)$$

If the system has reset, as in the case of the interval between points b and c , the measurement calibration is performed by adding the voltage change from b to the preset and from the reset to c .

$$(preset - b) + |(reset - c)| \equiv \text{one fringe} \quad (4.2)$$

When the known voltage value for one fringe is consistent this method can be used for converting voltage to distance. Depending on the slope of the measurement the calculated distance has a positive or negative sign which indicates the direction of travel. In the case the movement is towards the lens, this decreases the distance so a negative sign would be added. There are four cases which have slightly different algorithms but the principle is always the same: Two cases are when no reset occurs, neither away nor towards, and the other two are when a reset occurs, either away or towards.

The second DAQ software is based on an interpolation between preset and reset. The system is shown to be linear between resets which means that the physical distance traveled between resets is constant.

In Figure 4.3, a measurement is taken at point e . By knowing the preset and reset levels the voltage changes Δx and Δy are calculated. As that $\Delta x + \Delta y$ is a fixed distance the values between them can be interpolated according to

$$\frac{\text{known distance} \cdot \Delta y}{\Delta x + \Delta y} = \text{interpolated distance from preset to } e \quad (4.3)$$

As for the analog calibration, the software has to determine the same four cases.

Numerical Aperture, NA (acceptance angle for light launched into the fibre)	0.11
V number of laser diode λ , V	3.908

4.2. Calculation of Laser Spot Size

The spot size of the laser is important for the accuracy of surface roughness measurements, as the sensor is unable to resolve surface features that are smaller than the laser spot diameter. The spot size change on a curved surface is shown in Figure 8.3 (b).

In order to measure the spot size three methods were implemented. First, a theoretical calculation; second computer modeling; and third experimental estimation.

4.2.1. Calculation Using Gaussian Beam Theory

The V number is a parameter that describes how many modes can propagate in a fibre. The spot size can be calculated theoretically by using Gaussian Beam Ray Transfer Matrix theory [1]. According to this theory, the setup of the GRIN lens has to be divided into the following three parts: the fibre, the GRIN lens, and a free-space (air) segment, as illustrated in Figure 4.4. To determine the spot size on the surface at point O, the spot size at the intermediary location, X, has to be known. Once this is known, the ray transfer matrix Y for the GRIN lens and the ray transfer matrix Z for the free space can be applied, which results in an estimate of the spot size at the surface.

The fibre in the probe is single-mode fibre (SMF 28) and has the characteristic properties detailed in Table 4.1.

Table 4.1: Fibre properties

Radius of the core, r	4.45 μm
Numerical Aperture, NA (acceptance angle for light launched into the fibre)	0.11
V number of laser diode λ , V	3.908

For the given fibre properties in Table 4.1 the spot size at X, the exit of the fibre, is 4.09 μm. As the V number is greater than 2.405, the fibre is multimode at the laser diode wavelength. Practice, however, shows that the light propagates in a single mode [4].

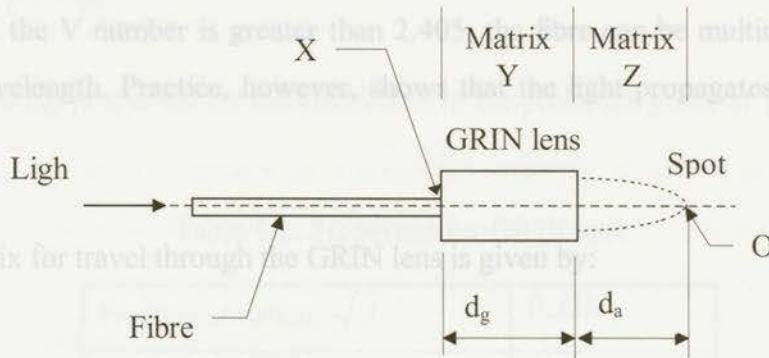


Figure 4.4: GRIN lens

$$\begin{pmatrix} A & B \\ C & D \end{pmatrix} = \begin{pmatrix} \cos(d_g \cdot \frac{n_1}{n_2}) & \frac{1}{\sqrt{n_2 \cdot n_1}} \sin(d_g \cdot \frac{n_1}{n_2}) \\ -\sqrt{n_2 \cdot n_1} \sin(d_g \cdot \frac{n_1}{n_2}) & \cos(d_g \cdot \frac{n_1}{n_2}) \end{pmatrix} \begin{pmatrix} \cos(d_a \cdot \frac{n_1}{n_2}) & \frac{1}{\sqrt{n_2 \cdot n_1}} \sin(d_a \cdot \frac{n_1}{n_2}) \\ -\sqrt{n_2 \cdot n_1} \sin(d_a \cdot \frac{n_1}{n_2}) & \cos(d_a \cdot \frac{n_1}{n_2}) \end{pmatrix} \quad (4.7)$$

The V number is a parameter that describes how many modes can propagate in a fibre. For a single-mode fibre, the V number is less than or equal to 2.405.

It is defined as [2]

$$V = \frac{2 \cdot \pi \cdot r}{\lambda} \cdot NA \quad (4.4)$$

$$NA = \sqrt{n_1^2 - n_2^2} \quad (4.5)$$

Where, the numerical aperture (NA) is given by where,

$$NA = \sqrt{(n_1)^2 - (n_2)^2} \quad (4.5)$$

n_1 = refractive index at a distance r from the optical axis
 n_2 and n_1 are the refractive indices of the fibre core and cladding respectively, r is the radius of the fibre core, and λ the wavelength of the laser diode, in this case 787 nm.

The single-mode spot size, ω_1 , of laser light propagating in a fibre of radius r and V number, is approximated by [3]

As a result of this parabolic index variation, a ray incident on the front surface follows a sinusoidal path along the rod lens. The period P_s of this sinusoidal path is called the "pitch" of the lens and is an important parameter in gradient index imaging. It is given by:

$$\omega_1 = \frac{r}{\sqrt{2 \cdot \log(V)}} \quad (4.6)$$

For the given fibre properties in Table 4.1 the spot size at X, the exit of the fibre, is 4.09 μm . As the V number is greater than 2.405, the fibre can be multimode at the laser diode wavelength. Practice, however, shows that the light propagates in a single mode [4].

The matrix for travel through the GRIN lens is given by:

Positive constant, \sqrt{A}	0.335
Refractive index at axis, n_3	1.6

$$\begin{pmatrix} A & B \\ C & D \end{pmatrix} = \begin{pmatrix} \cos\left(d_g \cdot \sqrt{\frac{n_4}{n_3}}\right) & \frac{1}{\sqrt{n_3 \cdot n_4}} \sin\left(d_g \cdot \sqrt{\frac{n_4}{n_3}}\right) \\ -\sqrt{n_3 \cdot n_4} \cdot \sin\left(d_g \cdot \sqrt{\frac{n_4}{n_3}}\right) & \cos\left(d_g \cdot \sqrt{\frac{n_4}{n_3}}\right) \end{pmatrix} \quad (4.7)$$

A more thorough description of ray transfer matrix theory can be found in the paper by Kogelnik and Li [1]. In a GRIN lens the index of the material varies parabolically as a function of the radius and may be expressed as [5]:

$$n = n_3 - \frac{1}{2} \cdot n_3 \cdot A \cdot r^2 \quad (4.8)$$

where, d_g is the distance from the end of the GRIN lens to the focused spot and is

d_g = length of the GRIN lens

n = refractive index at a distance r from the optical axis

n_3 = design index on the optical axis

$n_4 = A \cdot n_3$

A = positive constant

As a result of this parabolic index variation, a ray incident on the front surface follows a sinusoidal path along the rod lens. The period P , of this sinusoidal path is called the "pitch" of the lens and is an important parameter in gradient index imaging. It is given by:

$$\begin{pmatrix} A & B \\ C & D \end{pmatrix} = \begin{pmatrix} P = \frac{2\pi}{\sqrt{A}} & 0.011 \\ -9.6\sqrt{A} & 1 \end{pmatrix} \quad (4.9)$$

The following properties for the GRIN lens of the probe are given in Table 4.2.

Table 4.2: Properties for GRIN lens

Positive constant, \sqrt{A}	0.335
Refractive index at axis, n_3	1.6
Length of GRIN lens, d_g	5.4 mm

With these known properties the refractive index n_4 is 0.17956.

The ray transfer matrix Z for travel through air is given by:

$$Z = \begin{pmatrix} A & B \\ C & D \end{pmatrix} = \begin{pmatrix} 1 & d_a \\ 0 & 1 \end{pmatrix} \quad (4.10)$$

where d_a is the distance from the end of the GRIN lens to the focused spot and is 7.6 mm.

After inserting the known parameters and multiplying both matrices, the ray transformation matrix of the system can be calculated.

$$\begin{pmatrix} A & B \\ C & D \end{pmatrix} = \begin{pmatrix} 1 & d_a \\ 0 & 1 \end{pmatrix} \cdot \begin{pmatrix} \cos\left(d_g \cdot \sqrt{\frac{n_2}{n_0}}\right) & \frac{1}{\sqrt{n_0 \cdot n_2}} \sin\left(d_g \cdot \sqrt{\frac{n_2}{n_0}}\right) \\ -\sqrt{n_0 \cdot n_2} \cdot \sin\left(d_g \cdot \sqrt{\frac{n_2}{n_0}}\right) & \cos\left(d_g \cdot \sqrt{\frac{n_2}{n_0}}\right) \end{pmatrix} \quad (4.11)$$

This theoretical method of using the ray transfer matrix gives a spot size of 37.19 μm .

$$\begin{pmatrix} A & B \\ C & D \end{pmatrix} = \begin{pmatrix} 1 & 0.011 \\ -9.696 \cdot 10^{-4} & 1 \end{pmatrix} \quad (4.12)$$

The Code V computer modeling software was used to verify the theoretical calculation. The system was analyzed for the effects of Gaussian beam propagation. The Gaussian beam contracts to a minimum diameter at the beam waist (i.e. where there is a planar wave front). At this point, the complex beam parameter, q_1 , used to describe the beam, is purely imaginary. As the beam exits the fibre, a waist is formed which can be described by q_1 , [6]

$$q_1 = j \cdot \frac{\pi \cdot (\omega_1)^2}{\lambda} \quad (4.13)$$

where ω_1 , is the spot size of the fibre.

The beam can be described after it travels through the GRIN lens and free space by q_2 where

$$q_2 = \frac{A \cdot q_1 + B}{C \cdot q_1 + D} \quad (4.14)$$

To experimentally determine the spot size, a knife edge was used. The apparatus is schematically shown in Figure 4.5. The knife is moved a known distance in front of the GRIN lens in the direction with a vertical micrometer. The distance between the knife and the lens is controlled through a translation stage which can be adjusted with a DC motor. However, as the motor is imprecise, accurate measurements of travel distances are not possible. A dial gauge

$$j \cdot \frac{\pi \cdot (\omega_2)^2}{\lambda} = \frac{A \cdot q_1 + B}{C \cdot q_1 + D} \quad (4.15)$$

$$\omega_2 = \frac{-(-1)^{\frac{3}{4}}}{\sqrt{\pi}} \cdot \sqrt{\lambda} \cdot \frac{\sqrt{A \cdot q_1 + B}}{\sqrt{C \cdot q_1 + D}} \quad (4.16)$$

$$\omega_2 = 3.71895 \cdot 10^{-5} - 3.6964 \cdot 10^{-5} j \quad (4.17)$$

This theoretical method of using the ray transfer matrix gives a spot size of 37.19 μm .

4.2.2. Computer Modeling of Ray Optics

The Code V computer modeling software was used to verify the theoretical calculation. The system was analyzed for the effects of Gaussian beam propagation. Based on the information given above, the program calculated a magnification of 4.24 using ray optics, giving a spot size of $37.72 \mu\text{m}$. In addition, the program was able to calculate the blur caused by the GRIN lens. For a fibre NA of 0.11 it calculated an *rms* image diameter of 0.8 microns and 100% encircled energy diameter of 1.8 microns for the blurred image of a perfect point source. In this case, the image is formed 7.6 mm from the end of the GRIN lens. Thus, according to the blur the spot size would increase by between 0.8 and 1.8 microns depending on the criteria of intensity and cut-off point, i.e. the spot size is between 39.2 and $41.32 \mu\text{m}$.

4.2.3. Knife Edge Experiment

To experimentally determine the spot size, a knife edge was used. The apparatus is schematically shown in Figure 4.5. The knife is moved a known distance in front of the GRIN lens in the *z*-direction with a vernier micrometer. The standoff distance *d* between the knife and the lens is controlled through a translation stage which can be adjusted with a DC motor. However, as the motor is imprecise, accurate measurements of travel distances were measured with a dial gauge.

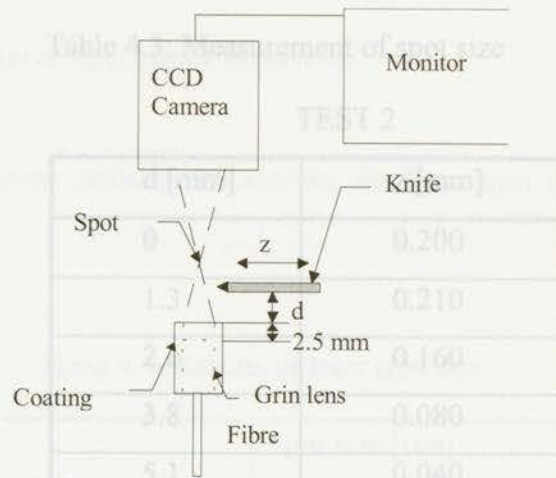


Figure 4.5: Knife edge experiment

On the monitor, a bright spot can be seen from the laser. As the knife edge is moved, the beam is cut off and the bright spot on the monitor from the CCD camera disappears. The spot size at the distance d is found by taking a reading on the vernier micrometer when the bright spot on the monitor starts to disappear, and by taking a second reading when the bright spot has just vanished. The difference between the two reading, is the spot size for the standoff distance, d . Table 4.3 gives the spot sizes for various standoff distances. The result is displayed in Figure 4.6.

The results indicate that the minimum spot of $40 \mu\text{m} \pm 1 \mu\text{m}$ occurs at a standoff distance of $5.15 \text{ mm} \pm 0.1 \text{ mm}$.



Figure 4.6: Laser spot size characteristics

Table 4.3: Measurement of spot size

TEST 2

d [mm]	z [mm]
0	0.200
1.3	0.210
2.6	0.160
3.8	0.080
5.1	0.040
5.5	0.050
6.8	0.100
8.1	0.220

Method	Spot size [µm]
Theoretical Calculations	3.19
Computer Modelling	3.2 - 4.3
Experimental Estimation	4.0

Each method is in reasonable agreement with the other methods and the experimentally determined values correspond well with the theoretical calculations. The spot size for the probe of this instrument is $\approx 40 \mu\text{m}$, and thus the resolution of a surface measurement is limited to $\approx 40 \mu\text{m}$. This compares unfavorably with the $12.5 \mu\text{m}$ standard stylus, the spot size of which is much smaller. There are several methods for achieving this, for example by using a smaller diameter fibre. The developers of the FIOSS are currently working on a method of using a telescopic arrangement of lenses that will give a spot size of $3.3 \mu\text{m}$.

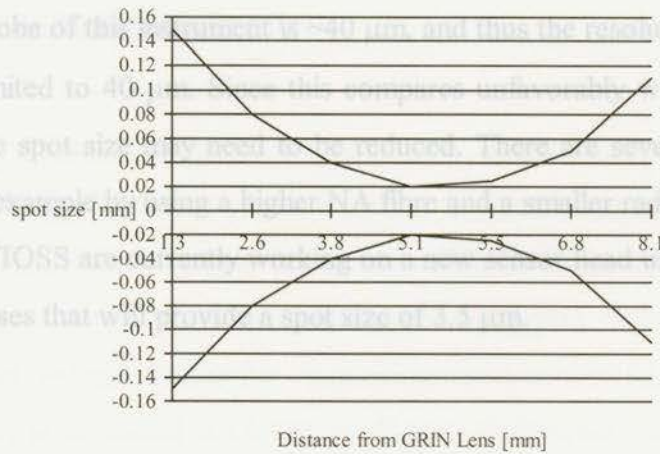


Figure 4.6: Laser spot size characteristics

4.2.4. Results of Laser Spot Size Calculation

The results of the three methods to calculate the laser spot size are shown in Table 4.4.

Table 4.4: Results of laser spot size

Method	Spot size [μm]
Theoretical Calculation	37.19
Computer Modeling	39.2 - 41.32
Experimental estimation	40

Each method is in reasonable agreement with the other methods and the experimentally determined values correspond well with the theoretical calculations. The spot size for the probe of this instrument is $\sim 40 \mu\text{m}$, and thus the resolution of a surface measurement is limited to $40 \mu\text{m}$. Since this compares unfavorably with the $12.5 \mu\text{m}$ standard stylus, the spot size may need to be reduced. There are several methods for achieving this, for example by using a higher NA fibre and a smaller radius of fibre. The developers of the FIOSS are currently working on a new sensor head using a telescopic arrangement of lenses that will provide a spot size of $3.5 \mu\text{m}$.

4.3. References

- The sensor system is controlled by a PC using LabVIEW, a program
- [1] Kogelnik, H. and T. Li. "Laser Beams and Resonators" *IEEE*, vol. 54, Oct. 1966: 1312-1329.
 - [2] Wilson, J. and J.F.B. Hawkes. *Laser Principles and Applications*. Prentice Hall International Series in Optoelectronics, 1987.
 - [3] Schneider, J. *Optical Waveguide Theory*. Chapman and Hall, 1983: 341.
 - [4] Domanski, A. W. and T. R. Wolinski, "Surface Roughness Measurement with Optical Fibers", *IEEE, Transactions on Instrumentation and Measurement*, vol. 41, no. 6, December 1992.
 - [5] Melles Griot, *Optics Guide 5*, 1995.

5.1. Analog Signal Calibration

The Analog Signal Calibration program was developed to determine the proportional relationship between a physical change in distance on a surface and the modulating voltage applied to the laser diode in the FOISS. For a chosen direction of travel, the program will find the reset and preset from the system. These levels are then used to calculate the voltage change for the physical move of one fringe from the MI when a reset occurs as explained in Chapter 4 "Sensor Calibration Theory". When no reset occurs, the change in voltage is the difference of voltage before and after the move of the fringe. Since the distance traveled for one fringe is known, the proportional relationship between voltage change and distance can be determined.

The flowchart of the program is graphically illustrated in Figure 5.1.

5. Data Acquisition Software

The sensor system is controlled by a PC using LabVIEW, a program development application similar to C or BASIC that is compatible with the data acquisition boards used in this work. LabVIEW uses a graphical programming language called 'G' to create programs in block diagram form. LabVIEW is a general-purpose programming system with comprehensive libraries of functions and subroutines for most programming tasks. It also permits sophisticated data acquisition and analysis. LabVIEW programs are called virtual instruments (VIs) because their appearance and operation imitate actual instruments but have an interactive user interface called the front panel. The VIs receive instructions from a block diagram constructed in G. The block diagram is a pictorial solution to a programming problem.

5.1. Analog Signal Calibration

The Analog Signal Calibration program was developed to determine the proportional relationship between a physical change in distance on a surface and the modulating voltage applied to the laser diode in the FOISS. For a chosen direction of travel, the program will find the reset and preset from the system. These levels are then used to calculate the voltage change for the physical move of one fringe from the MI when a reset occurs as explained in Chapter 4 "Sensor Calibration Theory". When no reset occurs, the change in voltage is the difference of voltage before and after the move of the fringe. Since the distance traveled for one fringe is known, the proportional relationship between voltage change and distance can be determined.

The flowchart of the program is graphically illustrated in Figure 5.1.

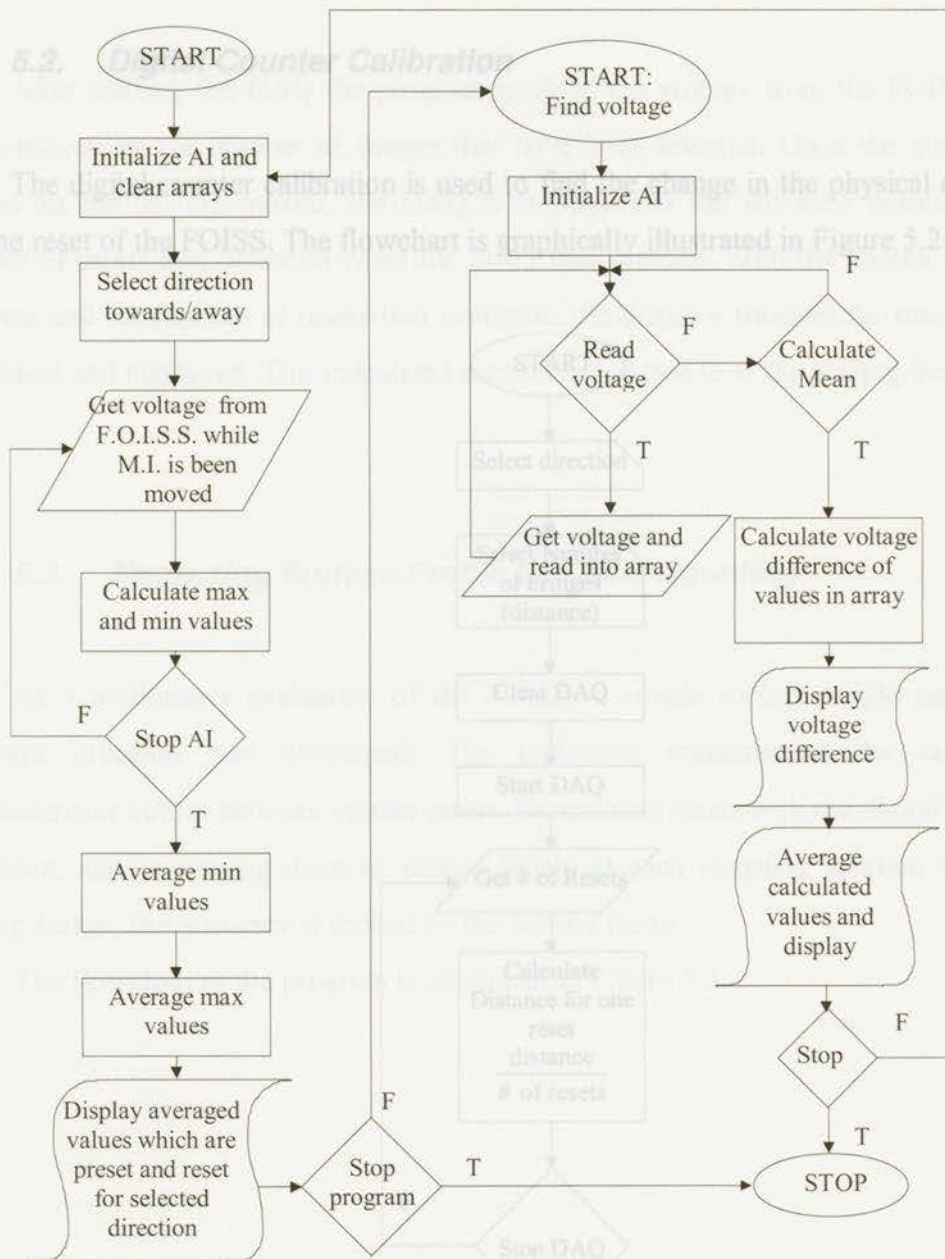


Figure 5.1: Flowchart, Analog Signal Calibration

Figure 5.2: Flowchart, Digital Counter Calibration

5.2. Digital Counter Calibration

After starting the DAQ the program reads in the voltage from the FOISS. The MI is moved by the number of fringes that have been selected. Once the number of fringes on the MI are moved, the DAQ is stopped and the software calculates the number of resets that occurred while the DAQ was running. With the known traveled distance and the number of resets that occurred, the distance traveled for one reset is calculated and displayed. This calculated value is stored to be used as the scaling factor.

5.3. Measuring Surface Profile with Interferometer Counting

As a preliminary evaluation of the simple surface height measuring software program was developed. The program implemented the consistent interferometer output between system resets with the digital counter extension, and converting them to surface height with each sampling location with the scaling factor. The accuracy is limited by the scaling factor.

The flowchart of the program is illustrated in Figure 5.3.

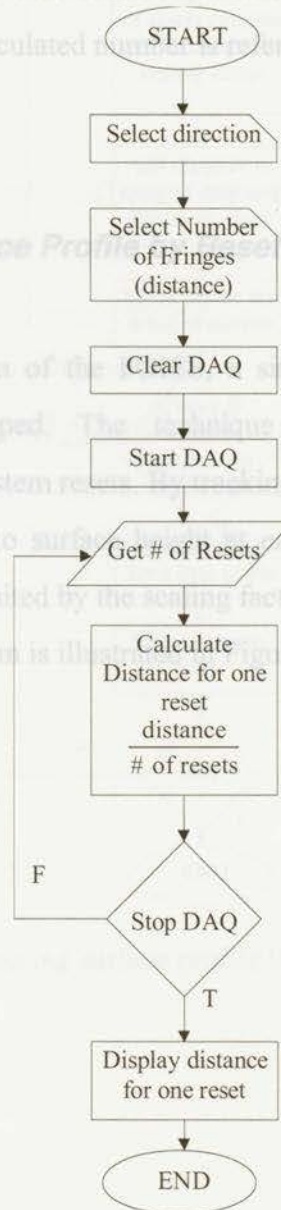


Figure 5.2: Flowchart, Digital Counter Calibration

After starting the DAQ the program reads in the voltage from the FOISS. The MI is moved by the number of fringes that have been selected. Once the number of fringes on the MI are moved, the DAQ is stopped and the software calculates the number of resets that occurred while the DAQ was running. With the known traveled distance and the number of resets that occurred, the distance traveled for one reset is calculated and displayed. This calculated number is referred to as the scaling factor.

5.3. Measuring Surface Profile by Reset Counting

As a preliminary evaluation of the FOISS, a simple surface height measuring software program was developed. The technique implemented the consistent interferometer output between system resets. By tracking resets with the digital counter extension, and converting them to surface height at each sampling location with the scaling factor. The accuracy is limited by the scaling factor.

The flowchart of the program is illustrated in Figure 5.3.

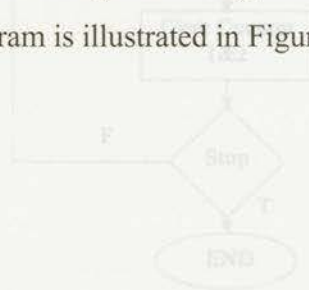


Figure 5.3: Flowchart, measuring surface profile by counting resets.

The LabVIEW program reads in the signal from the two counters. Counter 1 is responsible for the reset, if the laser waves closer to the lens, while Counter 2 is responsible for the reset, as the laser waves away from the lens. If resets are detected the scaling factor gets multiplied by the number of resets counted. Depending on the direction, the value is added or subtracted from the last height calculated. The new calculated value is appended to an array of data and displayed on a graph.

5.4. Measuring Surface Profile Resolution

The FOISS was proven to be linear between the distance and the number of resets. Hence, the measured signal from the FOISS can be interpolated between preset and preset level. This was implemented in the following program. The program measures the distances between resets. This permitted improved accuracy and resolution in the measurement of surface profile. The flowchart in Figure 5.4 graphically illustrates the program.

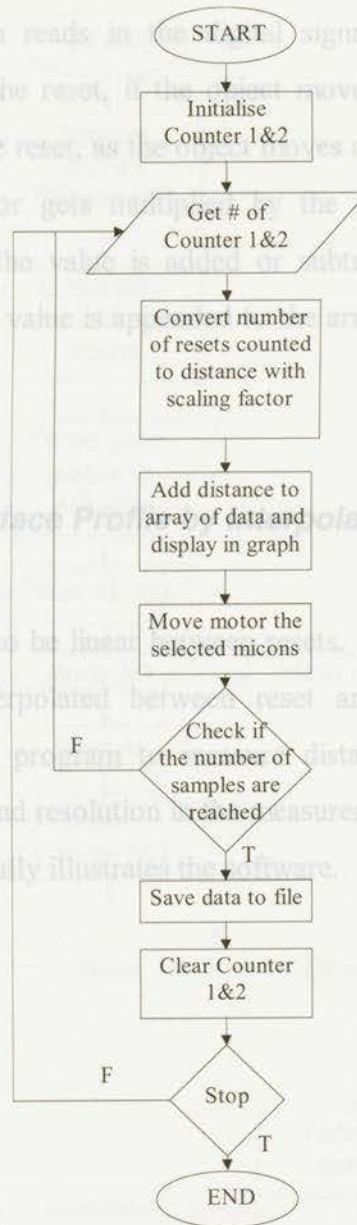
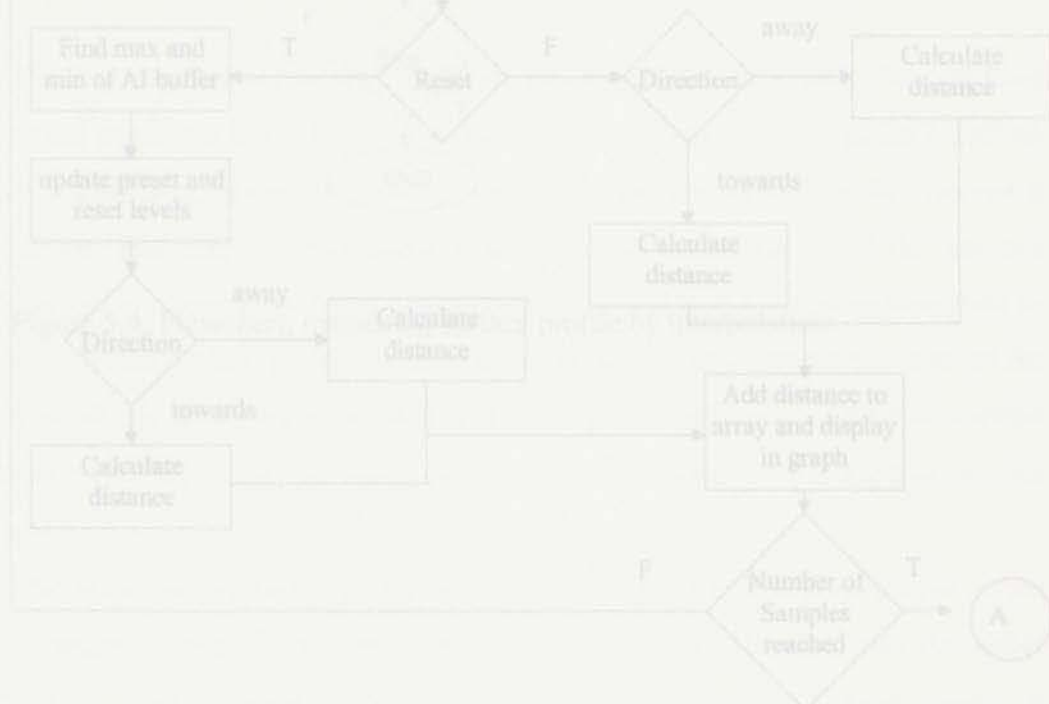


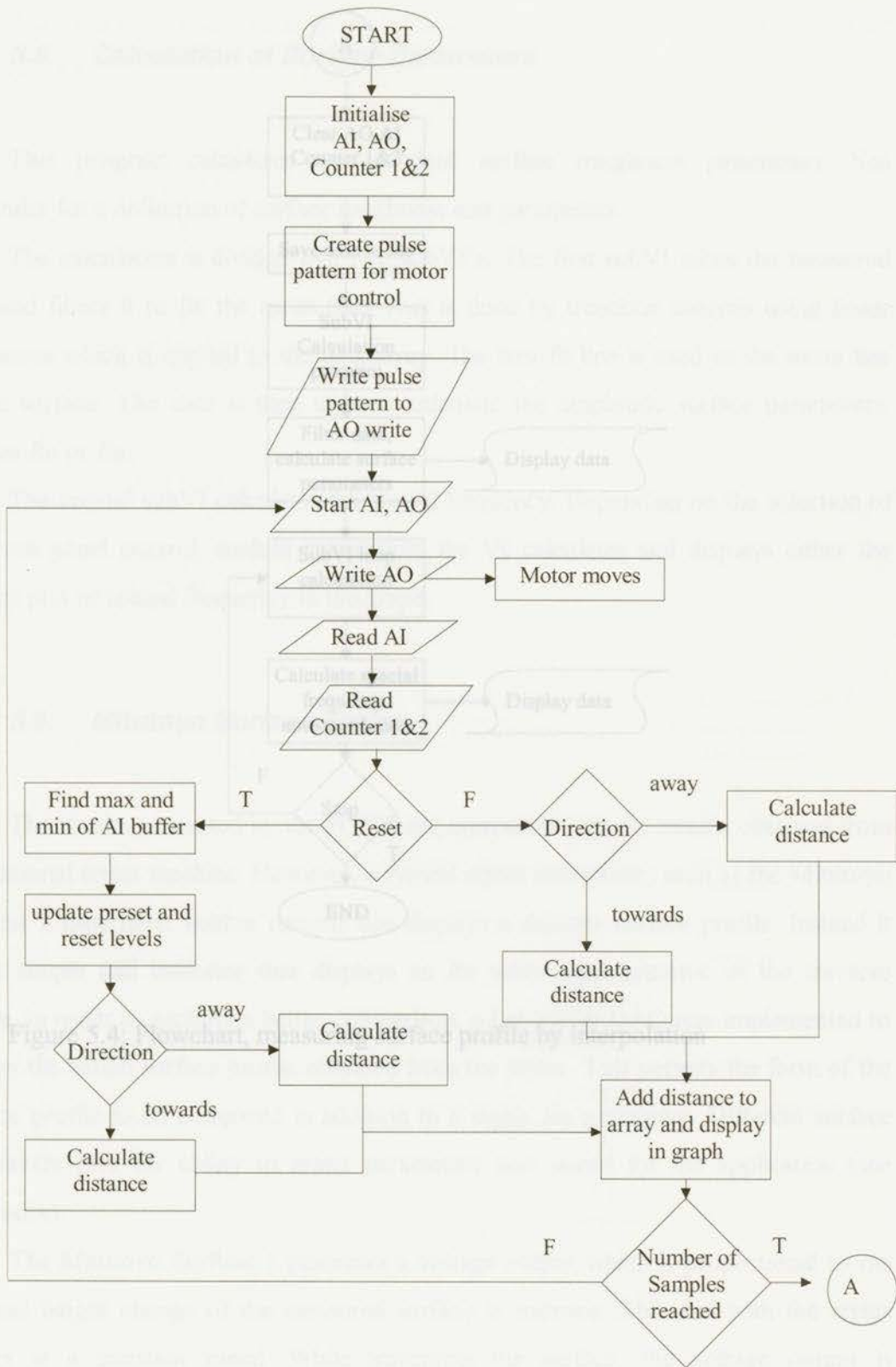
Figure 5.3: Flowchart, measuring surface profile by counting resets

The LabVIEW program reads in the digital signal from the two counters. Counter 1 is responsible for the reset, if the object moves closer to the lens, while Counter 2 is responsible for the reset, as the object moves away from the lens. If resets are detected the scaling factor gets multiplied by the number of resets counted. Depending on the direction, the value is added or subtracted from the last height calculated. The new calculated value is appended to the array of data and displayed on a graph.

5.4. Measuring Surface Profile by Interpolation

The FOISS was proven to be linear between resets. Hence, the measured signal from the FOISS can be interpolated between reset and preset level. This was implemented in the following program to measure distances between resets. This permitted improved accuracy and resolution in the measurement of surface profile. The flowchart in Figure 5.4 graphically illustrates the software.





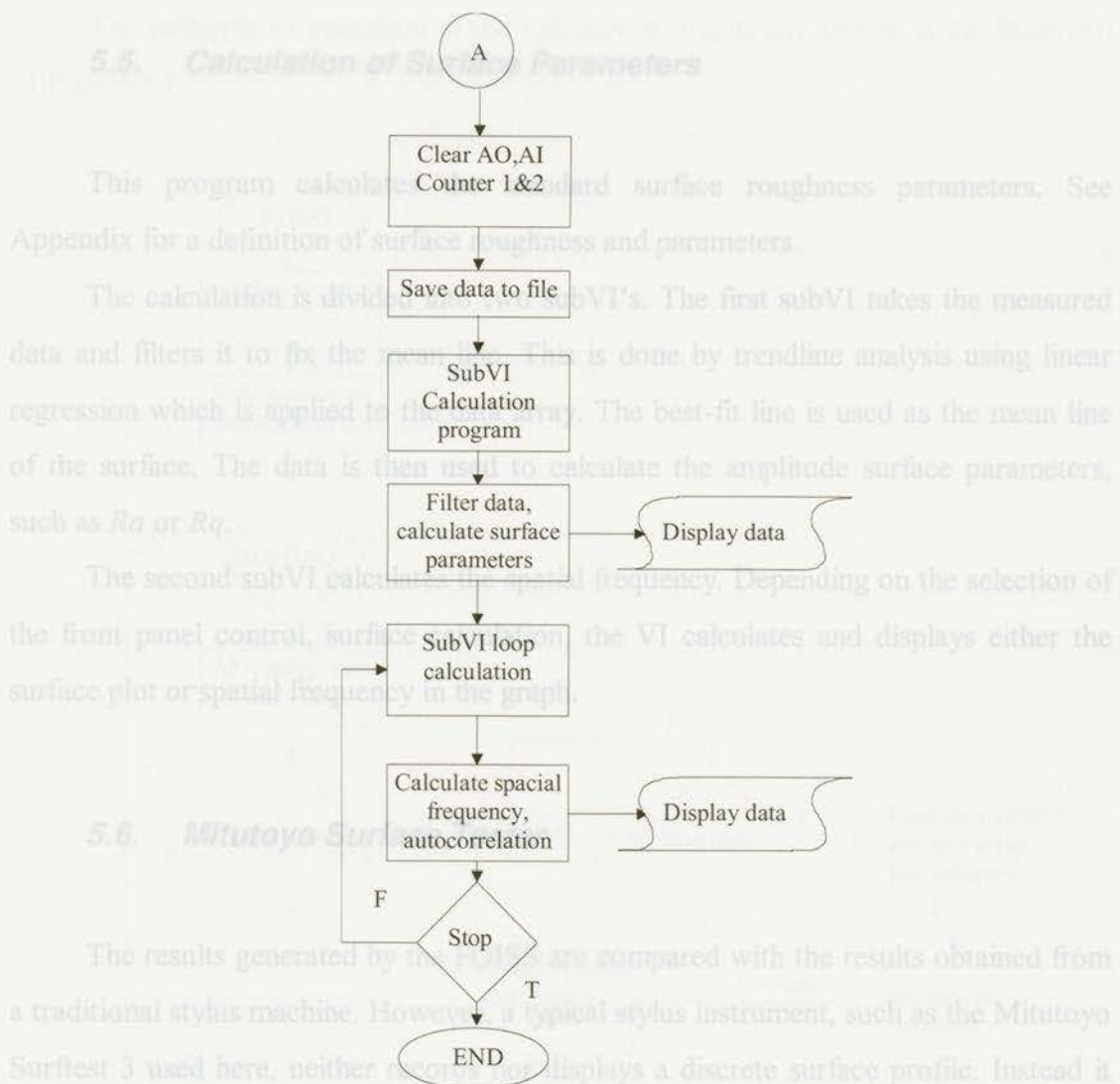


Figure 5.4: Flowchart, measuring surface profile by interpolation

The results generated by the software are compared with the results obtained from a traditional stylus machine. However, a typical stylus instrument, such as the Mitutoyo Surftest 3 used here, neither records nor displays a discrete surface profile. Instead it has a simple dial indicator that displays an R_a value representative of the traverse length. In order to perform a better comparison, a LabVIEW DAQ was implemented to display the actual surface profile obtained from the stylus. This permits the form of the surface profile to be compared in addition to a single R_a parameter. Different surface parameters give the ability to select parameters best suited for the application (see Appendix).

The Mitutoyo Surftest 3 generates a voltage output which is proportional to the physical height change of the measured surface in microns. The skid with the stylus moves at a constant speed. While traversing the surface, the voltage output is periodically sampled, and the distance of travel can be calculated.

5.5. Calculation of Surface Parameters

This program calculates the standard surface roughness parameters. See Appendix for a definition of surface roughness and parameters.

The calculation is divided into two subVI's. The first subVI takes the measured data and filters it to fix the mean line. This is done by trendline analysis using linear regression which is applied to the data array. The best-fit line is used as the mean line of the surface. The data is then used to calculate the amplitude surface parameters, such as R_a or R_q .

The second subVI calculates the spatial frequency. Depending on the selection of the front panel control, surface calculation, the VI calculates and displays either the surface plot or spatial frequency in the graph.

5.6. Mitutoyo Surface Tester

The results generated by the FOISS are compared with the results obtained from a traditional stylus machine. However, a typical stylus instrument, such as the Mitutoyo Surftest 3 used here, neither records nor displays a discrete surface profile. Instead it has a simple dial indicator that displays an R_a value representative of the traverse length. In order to perform a better comparison, a LabVIEW DAQ was implemented to display the actual surface profile obtained from the stylus. This permits the form of the surface profile to be compared in addition to a single R_a parameter. Different surface parameters give the ability to select parameters best suited for the application (see Appendix).

The Mitutoyo Surftest 3 generates a voltage output which is proportional to the physical height change of the measured surface in microns. The skid with the stylus moves at a constant speed. While traversing the surface, the voltage output is periodically sampled, and the distance of travel can be calculated.

The principle of operation of the software is graphically shown in the flowchart of Figure 5.5.

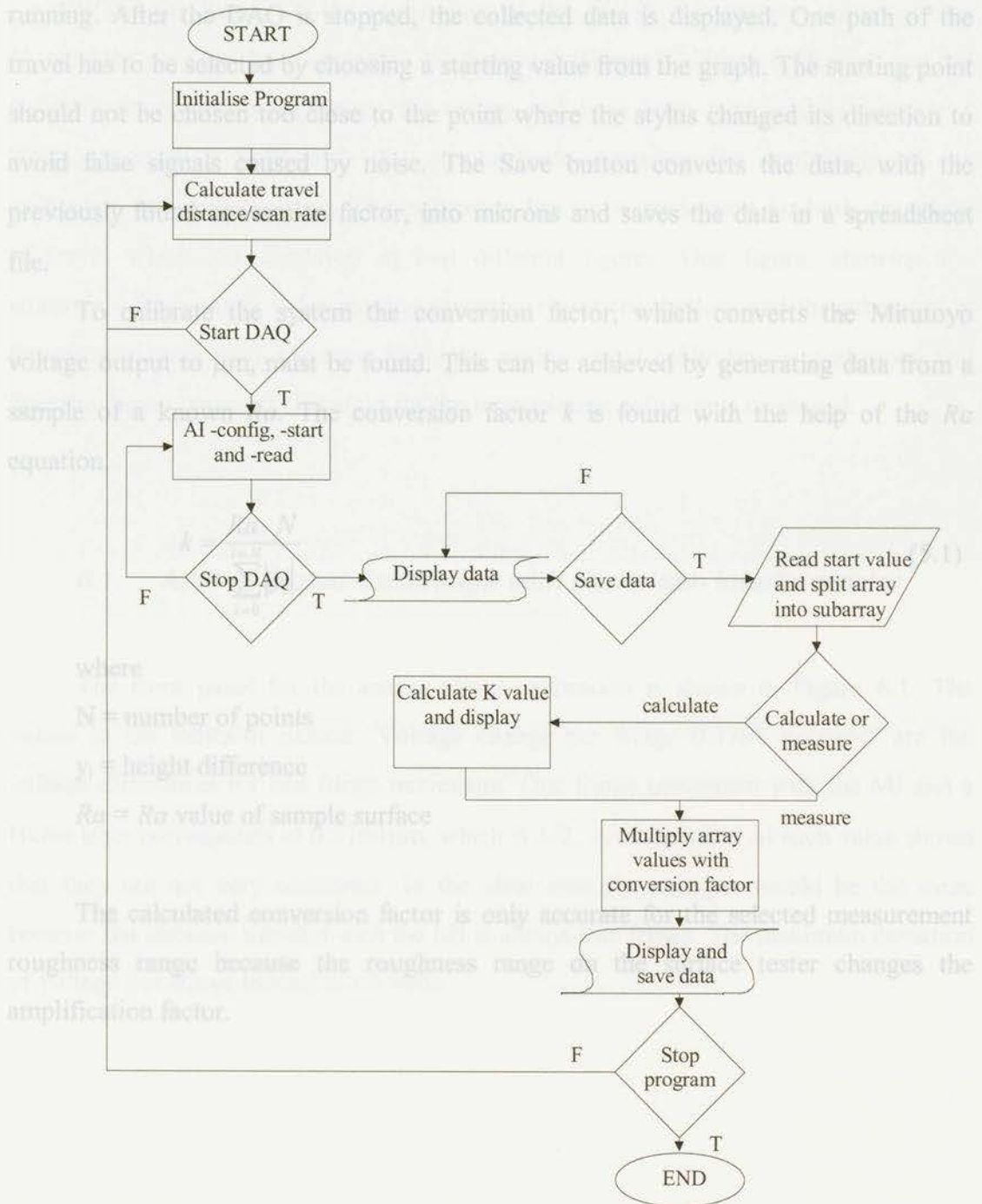


Figure 5.5: Flowchart, Mitutoyo Surface Tester

The power drive of the Mitutoyo Surf Tester causes the stylus to travel back and forth over the surface. The software reads in all the data while the power drive is running. After the DAQ is stopped, the collected data is displayed. One path of the travel has to be selected by choosing a starting value from the graph. The starting point should not be chosen too close to the point where the stylus changed its direction to avoid false signals caused by noise. The Save button converts the data, with the previously found conversion factor, into microns and saves the data in a spreadsheet file.

To calibrate the system the conversion factor, which converts the Mitutoyo voltage output to μm , must be found. This can be achieved by generating data from a sample of a known Ra . The conversion factor k is found with the help of the Ra equation.

$$k = \frac{Ra \cdot N}{\sum_{i=0}^{i=N} |y_i|} \quad (5.1)$$

where

N = number of points

y_i = height difference

Ra = Ra value of sample surface

The calculated conversion factor is only accurate for the selected measurement roughness range because the roughness range on the surface tester changes the amplification factor.

6. Sensor Calibration Measurement

While the theory of the conversion of the FOISS's integrator output to the physical distance has been explained in Chapter 4 "Sensor Calibration Theory" and the software programs to implement the theory and have been explained in Chapter 5 "Data Acquisition Software", this chapter now describes the application of the calibration software program. The calibration has to be performed for both directions of travel which are displayed in two different figures. One figure, showing the software's front panel, is for moving towards (closer to) the lens and the other one is for moving away from the lens. First, the analog signal calibration is performed and then the digital counter calibration for the interpolation software is displayed.

6.1. Analog Signal Calibration with Michelson Interferometer

Figure 6.1: Analog signal calibration towards

The front panel for the analog signal calibration is shown in Figure 6.1. The values in the indicator named "Voltage change per fringe 0.3164 microns" are the voltage differences for one fringe movement. One fringe movement with the MI and a HeNe laser corresponds to $0.3164\mu\text{m}$, which is $\lambda/2$. A comparison of each value shows that they are not very consistent. In the ideal case the voltages would be the same because the distance traveled with the MI is always one fringe. The maximum deviation of voltage per fringe moved is 1.3 volts.

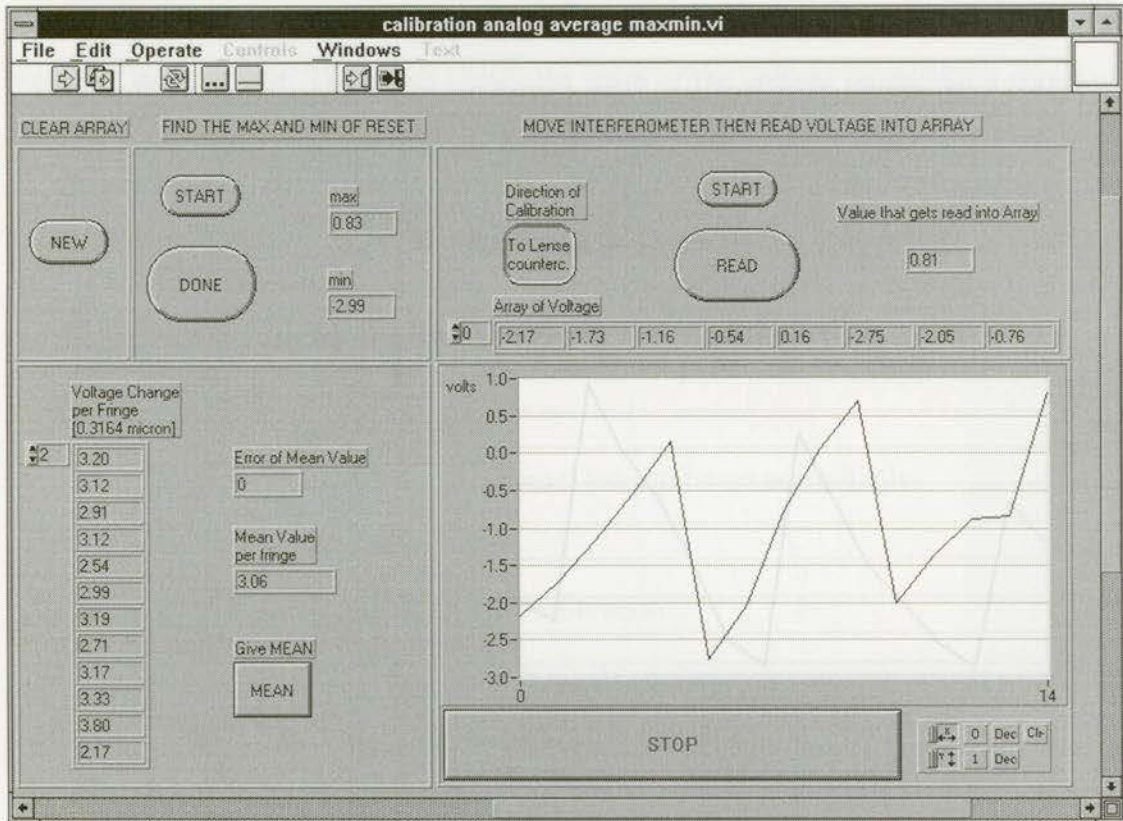


Figure 6.1: Analog signal calibration towards

In Figure 6.2 the voltage changes for moving away from the lens can be seen. The same pattern in the variation of the voltages occurred. $0.14\mu\text{m}$. For this reason, a different approach was developed; the digital counter calibration.

8.2. Digital Counter Calibration with Michelson Interferometer

The digital counter calculates the distance traveled by the object between resets. The sensor is arranged as illustrated in Figure 4.1 and the software program values indicated in Table 6.1 have to be set accordingly.

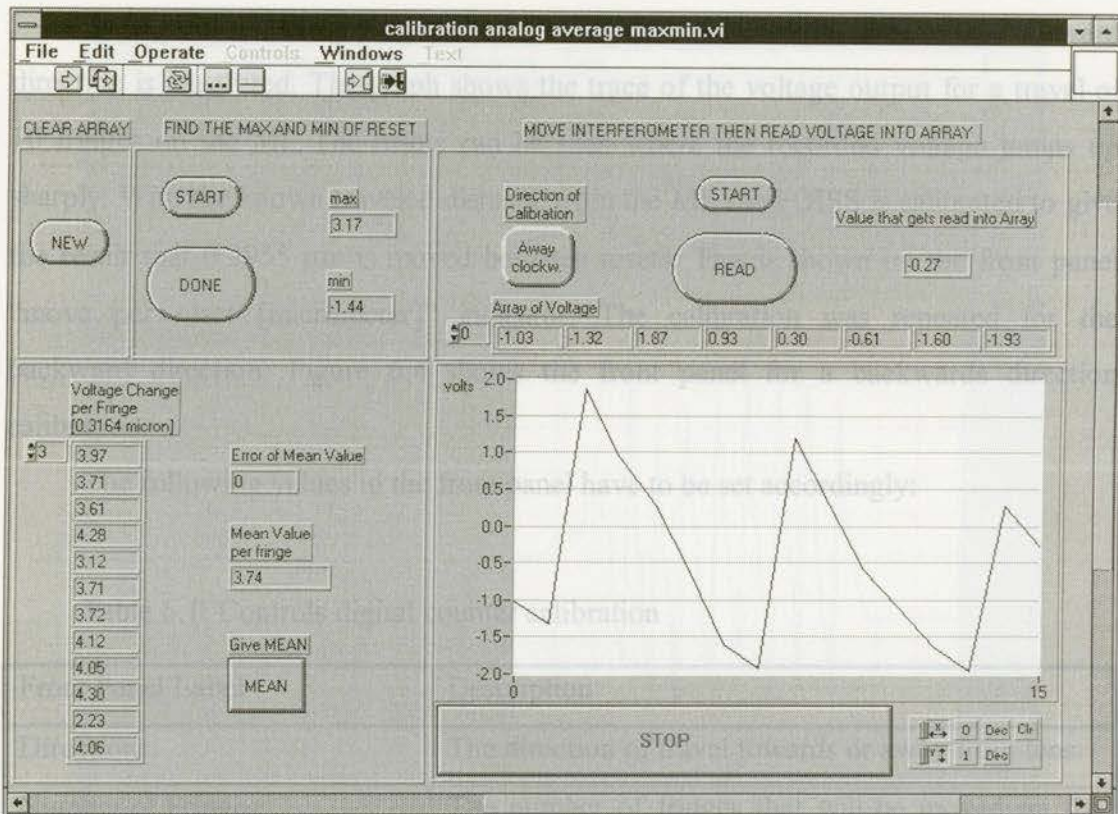


Figure 6.2: Analog signal Calibration away

This random fluctuation is not acceptable for an accurate measuring device. A system with such variations would only be accurate to $0.14\mu\text{m}$. For this reason, a different approach was developed: the digital counter calibration.

6.2. Digital Counter Calibration with Michelson Interferometer

The digital counter calculates the distance traveled by the object between resets. The sensor is arranged as illustrated in Figure 4.1 and the software program values indicated in Table 6.1 have to be set accordingly.

In Figure 6.3, the front panel after a digital counter calibration for the forward direction is illustrated. The graph shows the trace of the voltage output for a travel of 10 fringes on the MI. The resets can be seen where the recorded voltage jumps up sharply. With the known traveled distance from the MI, the FOISS is calibrated to give the result that $0.3955 \mu\text{m}$ is moved between resets. This is shown on the front panel “move per reset [micrometer]” indicator. The calibration was repeated for the backward direction. Figure 6.4 shows the front panel for a backwards direction calibration.

The following values in the front panel have to be set accordingly:

Table 6.1: Controls digital counter calibration

Front Panel Label	Description
Direction:	The direction of travel towards or away from lens.
Number of Fringes:	The number of fringes that will be moved on the MI.

Figure 6.3: Digital counter calibration towards

The distance traveled per reset was consistently found in both directions to be $0.3955 \mu\text{m}$. By knowing that the physical distance traveled between resets is always the same, the measured voltage values between the resets can be linearly interpolated to give accurate distance measurements.

The distance measured between resets is always the same, the measured voltage values between the resets can be linearly interpolated to give accurate distance measurements. The distance measured between resets is always the same, the measured voltage values between the resets can be linearly interpolated to give accurate distance measurements. The distance measured between resets is always the same, the measured voltage values between the resets can be linearly interpolated to give accurate distance measurements.

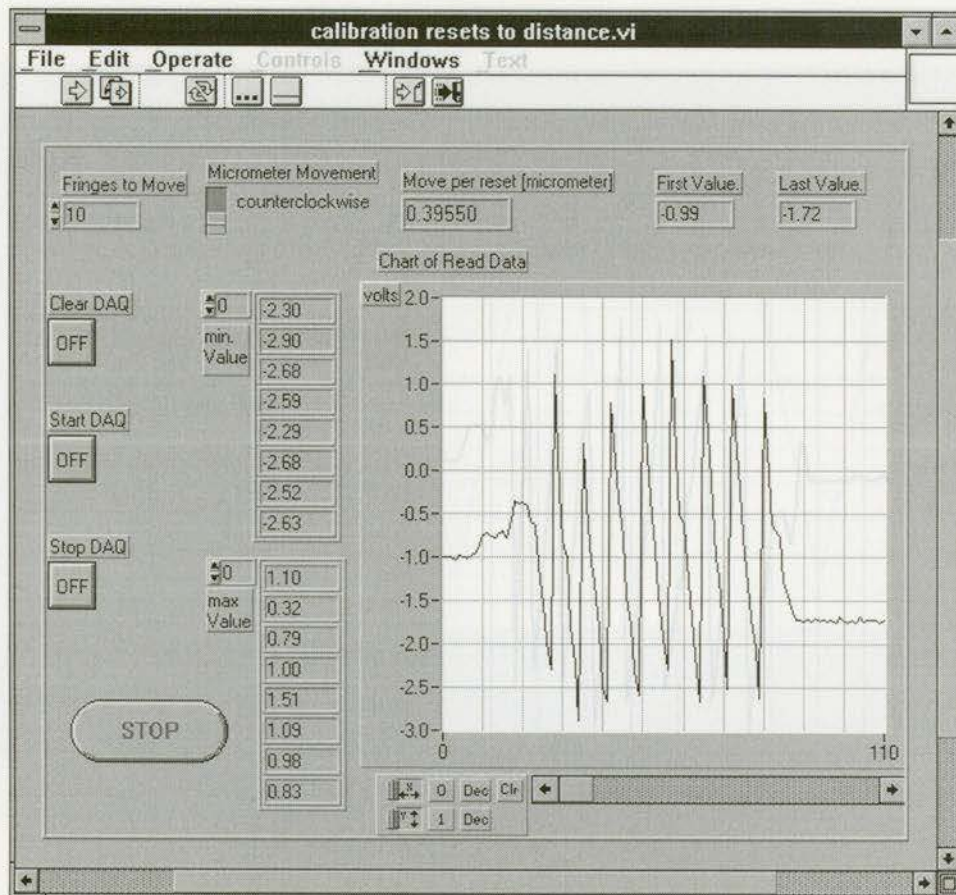


Figure 6.3: Digital counter calibration towards

The distance traveled per reset was consistently found in both directions to be $0.3955 \mu\text{m}$. By knowing that the physical distance traveled between resets is always the same, the measured voltage values between the resets can be linearly interpolated to give accurate distance measurements.

The software program "Measuring Surface Profile by Interpolation" has been used to determine how accurate the program and the system work together. The setup of the measurement is the same as in the sensor calibration with the MI. The software has been used to move the MI mirror one fringe away from the GRIN lens and then back to its starting point. This process has been repeated 10 times. The distance moved versus fringe is illustrated in Figure 6.5, while the measured values are summarized in Table 6.3.

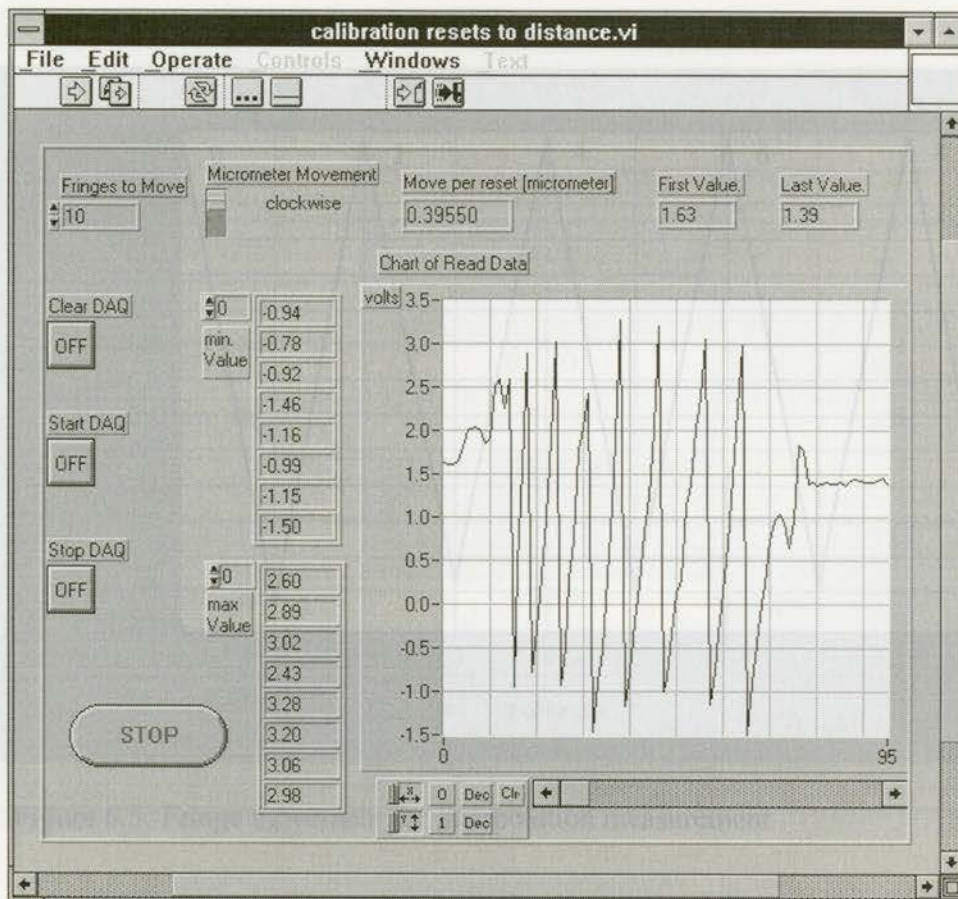


Figure 6.4: Digital counter calibration away from the position in the graph.

6.2.1. Accuracy of Interpolation

The software program “Measuring Surface Profile by Interpolation” has been used to determine how accurate the program and the system work together. The setup of the measurement is the same as in the sensor calibration with the MI. The software has been used to move the MI mirror one fringe away from the GRIN lens and then back to its starting point. This process has been repeated 10 times. The distance moved versus fringe is illustrated in Figure 6.5, while the measured values are summarized in Table 6.2.

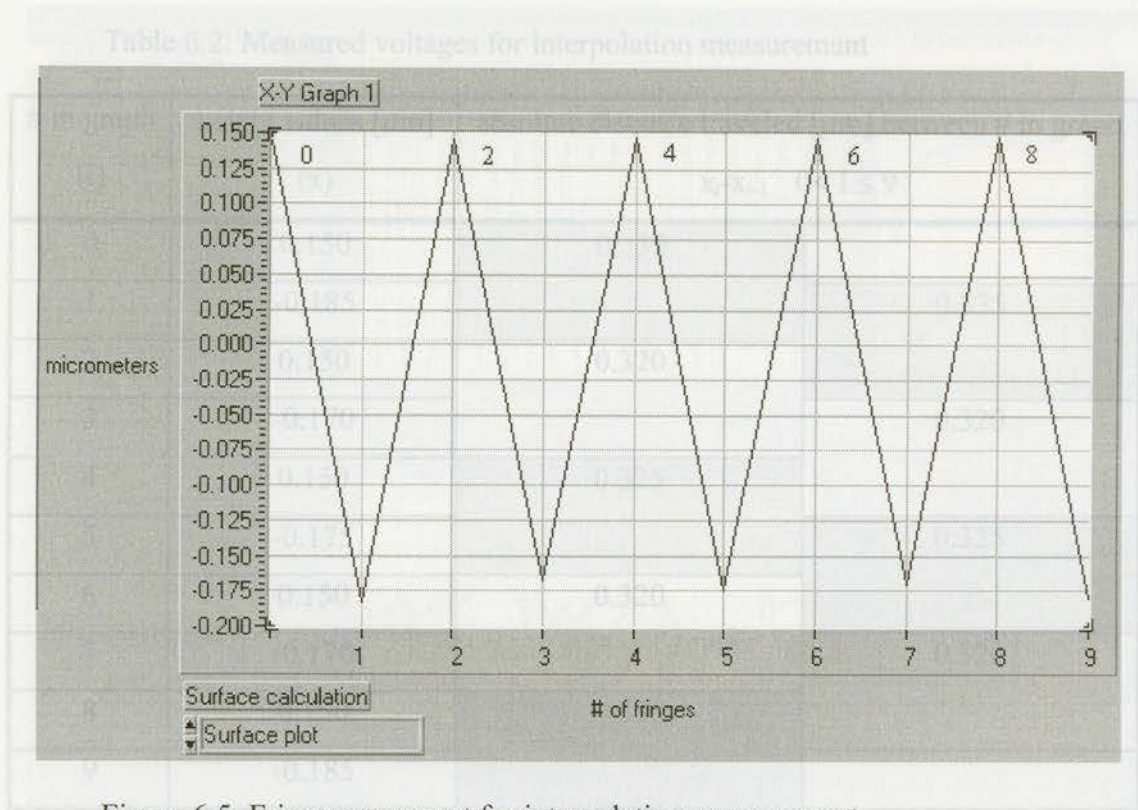


Figure 6.5: Fringe movement for interpolation measurement

The mean of the 9 traveled distances is $0.326 \pm 0.007 \mu\text{m}$. This is an error of 3%.

The numbers 0 through 9 are used to refer to the position in the graph.

6.2.2. Accuracy of Mitutoyo Surface Tester

2.2. Sensor Operating Time: Results

A DAQ software program has been written to collect the data from the Mitutoyo surface tester. This data could be fed into the interpolation program to calculate the surface parameters. The front panel of the data interpolation software with the data from a calibration sample is illustrated in Figure 6.6. The calibration sample which is supplied by Mitutoyo has a known R_a of 2.95 and a profile amplitude of 9.0 μm . The values produced by the program were consistent with the calibration sample.

Resolution = 0.200 μm

Mean of 1000 = 2.95 μm

Table 6.2: Measured voltages for interpolation measurement

# in graph (i)	height values [μm] (x)	absolute distance traveled [μm] between # in graph $x_i - x_{i-1} \quad 0 < i \leq 9$
0	0.150	0.335
1	-0.185	0.335
2	0.150	0.320
3	-0.170	0.320
4	0.150	0.325
5	-0.175	0.325
6	0.150	0.320
7	-0.170	0.320
8	0.150	0.335
9	-0.185	

The mean of the 9 traveled distances is $0.326 \pm 0.007 \mu\text{m}$. This is an error of 3%.

6.2.2. Accuracy of Mitutoyo Surface Tester

6.3. Sensor Operating Specifications

A DAQ software program has been written to collect the data from the Mitutoyo surface tester. This data could be fed into the interpolation program to calculate the surface parameters. The front panel of the data interpolation software with the data from a calibration sample is illustrated in Figure 6.6. The calibration sample which is supplied by Mitutoyo has a known Ra of 2.95 and a profile amplitude of $9.0 \mu\text{m}$. The values produced by the program were consistent with the calibration sample.

Resolution = $0.007 \mu\text{m}$

Standoff distance = 5.15 mm

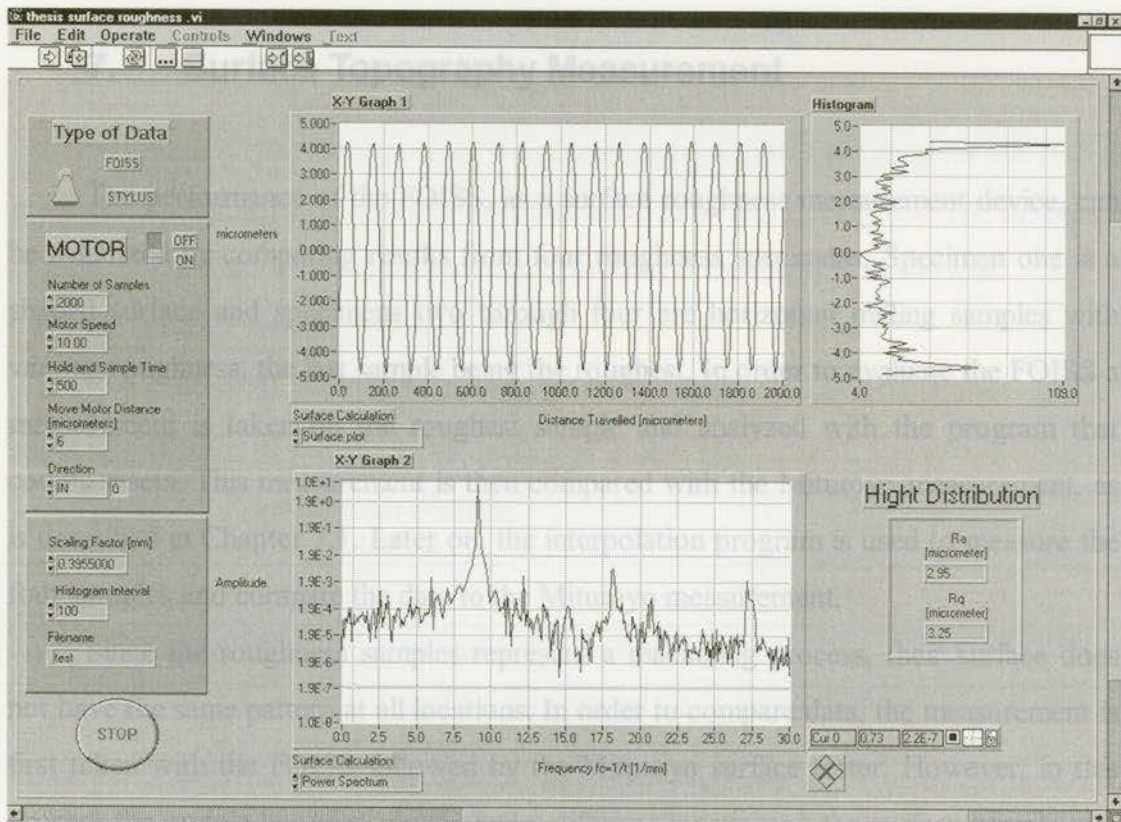


Figure 6.6: Accuracy of the Mitutoyo Surface Tester

both devices. Therefore, it is to be expected that there will be local differences when the comparison of the two surface measurements is made. The general results for each sample, however, should be similar. This is a universal problem in surface roughness measurement even with the

6.3. Sensor Operating Specifications

After the system had been evaluated, the operating specifications of the FOISS were determined to be:

Depth of field = $\pm 500 \mu\text{m}$

Spot diameter = $40 \mu\text{m}$

Resolution = $0.007 \mu\text{m}$

Standoff distance = 5.15 mm

The counting software has been developed for the evaluation of the FOISS as a surface measuring device. It moves the sample in selected intervals and counts the number of resera that occur. Using the scaling factor, the measured values are converted to μm and the profile is plotted in the graph. There is no filtering or surface parameter calculation performed on the collected surface profile data.

7. Surface Topography Measurement

The performance of the FOISS, as a surface roughness measurement device, can be evaluated by comparing results from four roughness specimens. Specimen one is a shaped surface and specimens two through four are horizontal milling samples with varying roughness, the last sample being the roughest. In order to evaluate the FOISS a measurement is taken on the roughest sample and analyzed with the program that counts resets. This measurement is then compared with the Mitutoyo measurement, as is described in Chapter 7.1. Later on, the interpolation program is used to measure the four samples and compare the data to the Mitutoyo measurement.

Since the roughness samples represent a machining process, their surface does not have the same pattern at all locations. In order to compare data, the measurement is first taken with the FOISS followed by the Mitutoyo surface tester. However, in this process the sample has been moved and a different location on the surface sample was measured. It is impossible to ensure the same location with both devices. Therefore, it is to be expected that there will be local differences when the comparison of the two surface measurements is made. The general results for each sample, however, should be similar. This is a universal problem in surface roughness measurement even with the stylus method.

7.1. Reset Counting Comparison

The reset counting software has been developed for the evaluation of the FOISS as a surface measuring device. It moves the sample in selected intervals and counts the number of resets that occur. Using the scaling factor, the measured values are converted to μm and the profile is plotted in the graph. There is no filtering or surface parameter calculation performed on the collected surface profile data.

7.1.1. Measuring Surface Profile by Reset Counting

In Figure 7.1 the front panel of the preliminary evaluation software for the FOISS is shown. A distance of 7 mm has been measured in 10 μm increments. The measured sample representing a horizontal machining process is the roughest of the four.

The front panel controls have to be set accordingly:

Table 7.1: Controls reset counting

Front Panel Label	Description
Number of Samples:	How many data points collected.
Motor Speed:	Speed between 1 and 10, 1 being the slowest and 10 the fastest.
Hold and Sample Time:	The number of milliseconds that the system should wait after the motor moved the sample, so that the vibration noise is reduced.
Move in μm :	Distance that the motor moves per sample.
Direction:	In or out of the motor spindle.
Filename:	File will be stored in the chosen file path.
Scaling factor:	Value in μm that equals one reset.

In Figure 7.2 the front panel of the Mitutoyo surface tester software is shown. The measured sample is the same one that was measured with the FOISS. Software parameters are set as in Table 7.2.

Software parameters are set as in Table 7.2.

Figure 7.2: Front panel Mitutoyo surface tester

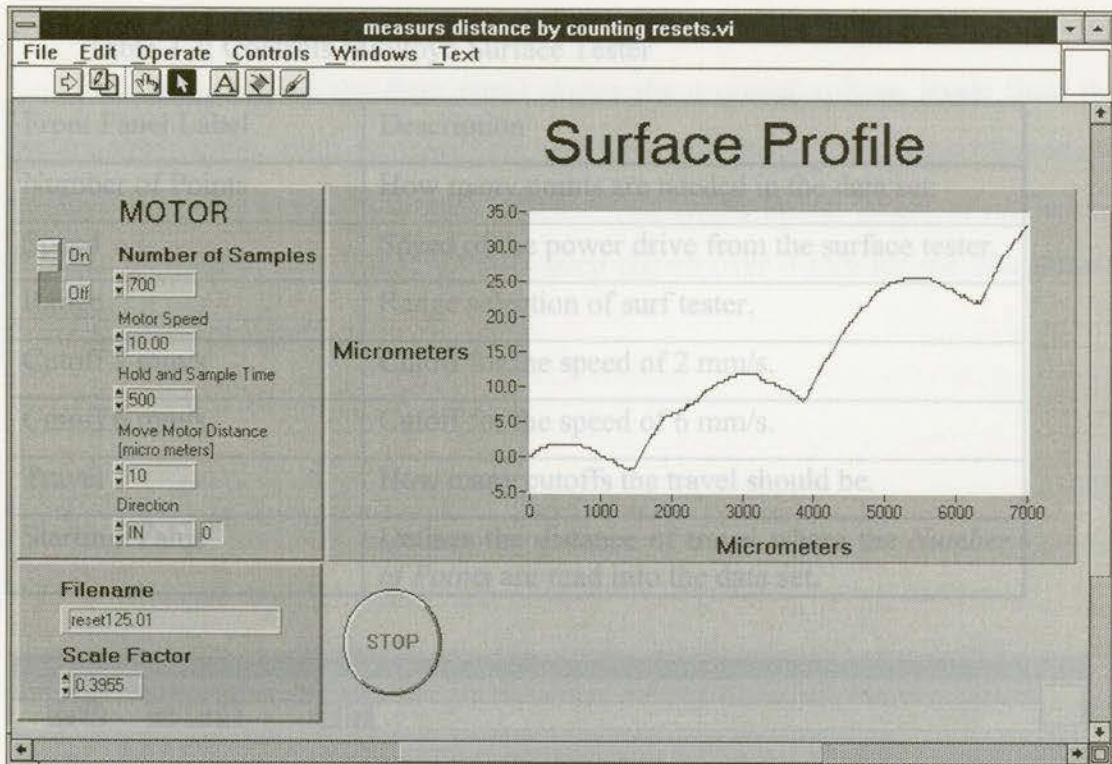


Figure 7.1: Front panel reset counting

7.1.2. Measuring Surface Profile with Mitutoyo Surface Tester

In Figure 7.2 the front panel of the Mitutoyo surface tester software is shown. The measured sample is the same one that was measured with the FOISS.

Software parameters are set as in Table 7.2.

Figure 7.2: Front panel Mitutoyo surface tester

Table 7.2: Controls Mitutoyo Surface Tester

Front Panel Label	Description
Number of Points	How many points are needed in the data set.
Speed	Speed of the power drive from the surface tester.
Range	Range selection of surf tester.
Cutoff 2 mm/s	Cutoff for the speed of 2 mm/s.
Cutoff 6 mm/s	Cutoff for the speed of 6 mm/s.
Travel	How many cutoffs the travel should be.
Starting Value	Defines the distance of travel where the <i>Number of Points</i> are read into the data set.

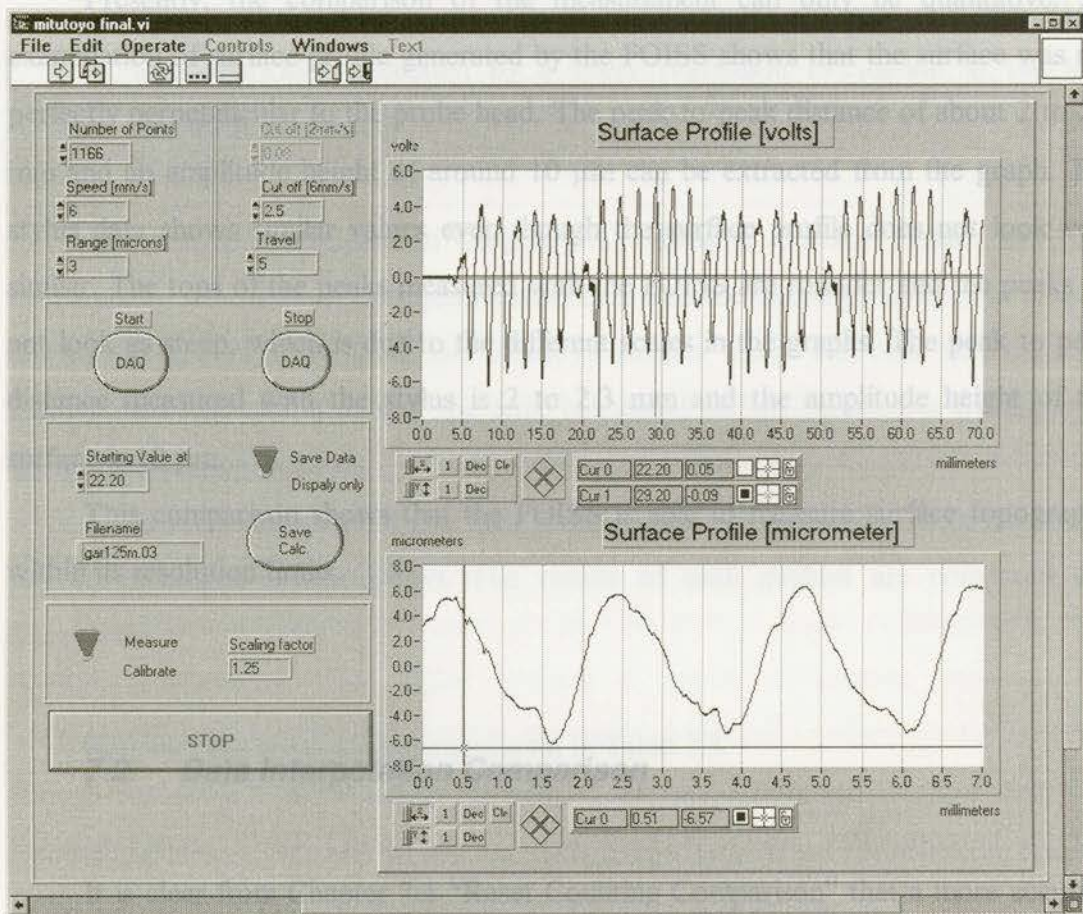


Figure 7.2: Front panel Mitutoyo surface tester

The top graph in the front panel shows the acquired voltage levels from the surface tester as the stylus traverses back and forth over the surface. The bottom graph displays the data samples converted with the conversion factor; height in μm versus distance traveled in mm. This graph has been shown over 7 mm for the comparison with the FOISS method.

2) The power spectrum, peak count, and other spatial parameters of the surface are not displayed by the profilometer.

3) A large-radius skid is used as a reference on the surface. The stylus measures the profile with respect to this reference as it rests on, and traverses the surface. This generates the general level of the surface. The FOISS does not

7.1.3. Comparison

Presently, the comparison of the measurement can only be qualitative. An examination of surface profile generated by the FOISS shows that the surface was not perfectly perpendicular to the probe head. The peak-to-peak distance of about 2 to 2.5 mm and an amplitude height of around 10 μm can be extracted from the graph. The stylus data shows similar values even though the surface profile does not look very similar. The tops of the peaks measured with the FOISS are rounder and the peaks do not look as steep, which is due to the different scales in the graphs. The peak to peak distance measured with the stylus is 2 to 2.3 mm and the amplitude height of the surface is 12 μm .

This comparison shows that the FOISS is able to measure surface topography within its resolution limits.

7.2. Data Interpolation Comparison

It is clear from Chapter 7.1 "Reset Counting Comparison" that a more accurate surface profile calculation technique is required. An improved technique for the comparison of the Mitutoyo data to the FOISS data has been developed. Furthermore,

parameters can be determined in the FOISS software that could not be obtainable with the stylus system. The limitations of the stylus measurement are:

Front Panel Label	Description
Type	
Number	1) The stylus only displays the R_a value on the dial gauge which is difficult to read accurately because it fluctuates back and forth as the stylus traverses the surface.
Motor speed	Speed between 1 and 10, 1 being the slowest and 10 the fastest.
Hold and Sample Time	The number of ms that the system should wait for the motor moved the sample, so that the
Move in μm	Distance that the motor moves per sample.
Direction	In or out of the motor spindle.
Filename	File name to store the data in the chosen file.
Scaling factor	Value to sum the counts to one gram.
Histogram Interval	Interval setting for the histogram.
Motor ON/OFF	Switches the motor on and off.

The software described in Chapter 5.6 “Mitutoyo Surface Tester” has been developed to record the surface profile measured with the Mitutoyo stylus. For a better comparison the data file from the Mitutoyo surface tester was read into the data interpolation software. This way the same calculated surface parameters are displayed for both measuring methods.

In the following sub-sections, four surface samples are measured with the FOISS and the Mitutoyo stylus system. The results of each method are compared and discussed.

Software parameters are set as shown in Table 7.3.

Table 7.3: Controls measuring surface profile by interpolation

Front Panel Label	Description
Type of Data	Takes a measurement with the FOISS or reads a saved file from the Mitutoyo stylus.
Number of Samples:	How many data points should be read.
Motor speed:	Speed between 1 and 10, 1 being the slowest and 10 the fastest.
Hold and Sample Time:	The number of <i>ms</i> that the system should wait after the motor moved the sample, so that the vibration noise gets reduced.
Move in μm :	Distance that the motor moves per sample.
Direction:	In or out of the motor spindle.
Filename:	File will get stored in the chosen file/path.
Scaling factor:	Value in μm that equals to one reset.
Histogram Interval:	Interval setting for the histogram.
Motor ON/OFF:	Switches the motor on and off.

Figure 7.3 shows the FOISS front panel software. The measured surface profile and surface spatial frequency power spectrum are shown in the top and bottom graph respectively. The surface data histogram and calculated R_a and R_q values of the profile are shown on the right of the panel. These values and graphs are used to compare the FOISS and the stylus measurements.

A surface displaying a regular profile can have a single (fundamental) or a number (fundamental plus higher orders) of spatial frequencies present. The fundamental frequency is related to the lay marks. A periodic surface can be identified from a spectrum with a certain pattern of discrete wavelength components. The histogram helps to distinguish between asymmetrical profiles of the same R_a and R_q . Functions and limitations of R_a and R_q are explained in Appendix A.

Sample #1

The first sample is manufactured by the shaping process - similar to turning on a lathe. The cutting tool is moved in a straight line over the surface as it removes material from the workpiece. On the next machining pass, the tool moves perpendicular to the lay direction by one increment (determined by the feed rate). These machining marks should be detectable on the surface profile. When a fingernail is run over the surface it is possible to detect the presence of feed marks but a quantitative answer can not be obtained. It is apparent that neither of these methods is accurate enough. Even though the surface feels and looks very smooth, feed marks are present due to the nature of the machining process.

The surface of the sample measured using the FOISS is illustrated in Figure 7.3 and the principle component of the surface spatial frequency is 0.87 mm^{-1} , which corresponds to a 1.14 mm peak-to-peak distance. The distinct peak of the fundamental frequency shows that the measured surface is periodic and hence these peaks can be identified as the lay marks. The surface amplitude of the three peaks varies from $1.0 \text{ }\mu\text{m}$ to $2.2 \text{ }\mu\text{m}$ and the calculated roughness average (Ra) is $0.42 \text{ }\mu\text{m}$. The surface profile waviness has random irregularities superimposed on it that can be related to the characteristics of the shaping process, for example tool vibration or chatter. The histogram shows a wide range of measured values that have a tendency towards the negative values. This can be interpreted as a slightly asymmetrical surface profile, indicating an abundance of surface peaks.

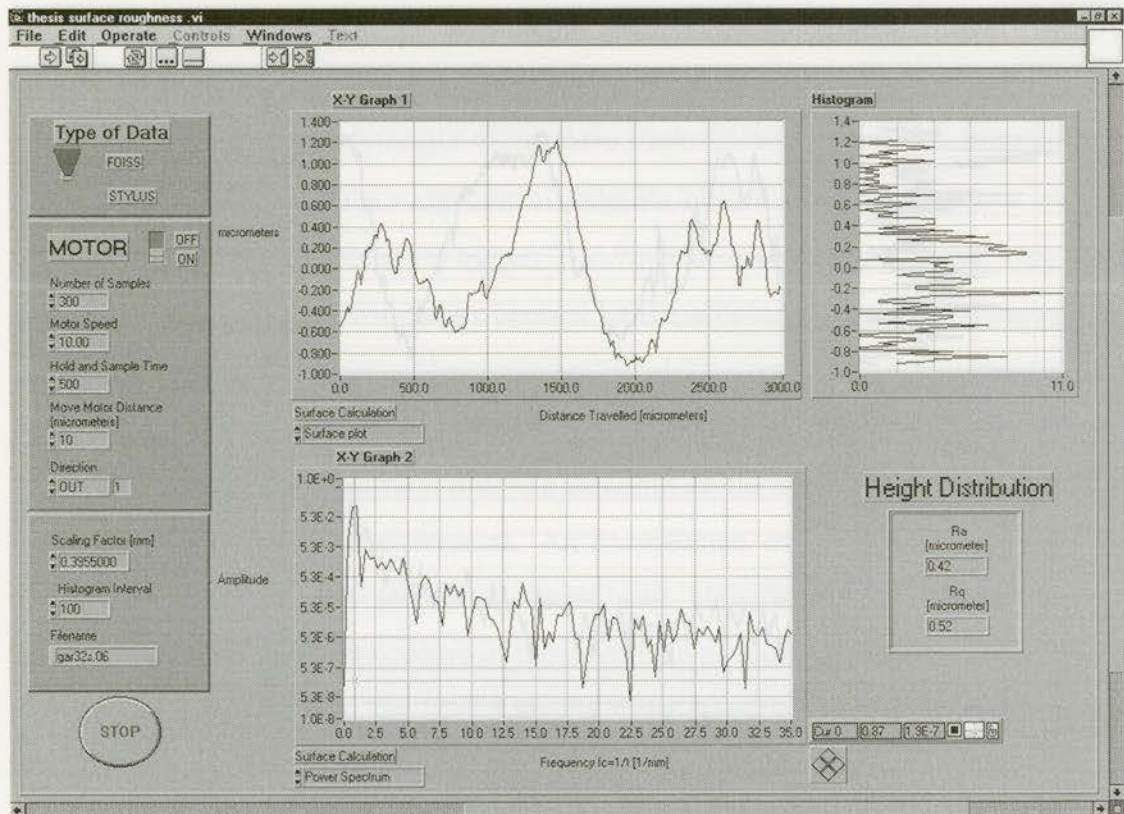


Figure 7.3: FOISS measurement, Sample #1

The Figure 7.4 shows the surface roughness measured using the Mitutoyo stylus software. to-peak distance. The measurement with the stylus indicates a wider spacing than the FOISS, which can be explained by the following two reasons: (1) The inaccuracy of the DC-motor translation stage system that positions the sample underneath the sensor head. The translation stage is moved against a spring which increases the motor load, with the result that the intended step is diminished. (2) The inaccuracies caused by a large laser spot size. The theory of the interferometer assumes that the strongest signal is the light reflected back from the center of the spot. If, for example, there is a strong reflection back into the probe from the edge of the spot, that swamps the signal from the center, the measurement will be referenced to the edge. This problem may be overcome by making the spot size smaller. Light reflected from different locations within the spot changes the measurement and the spatial parameter.

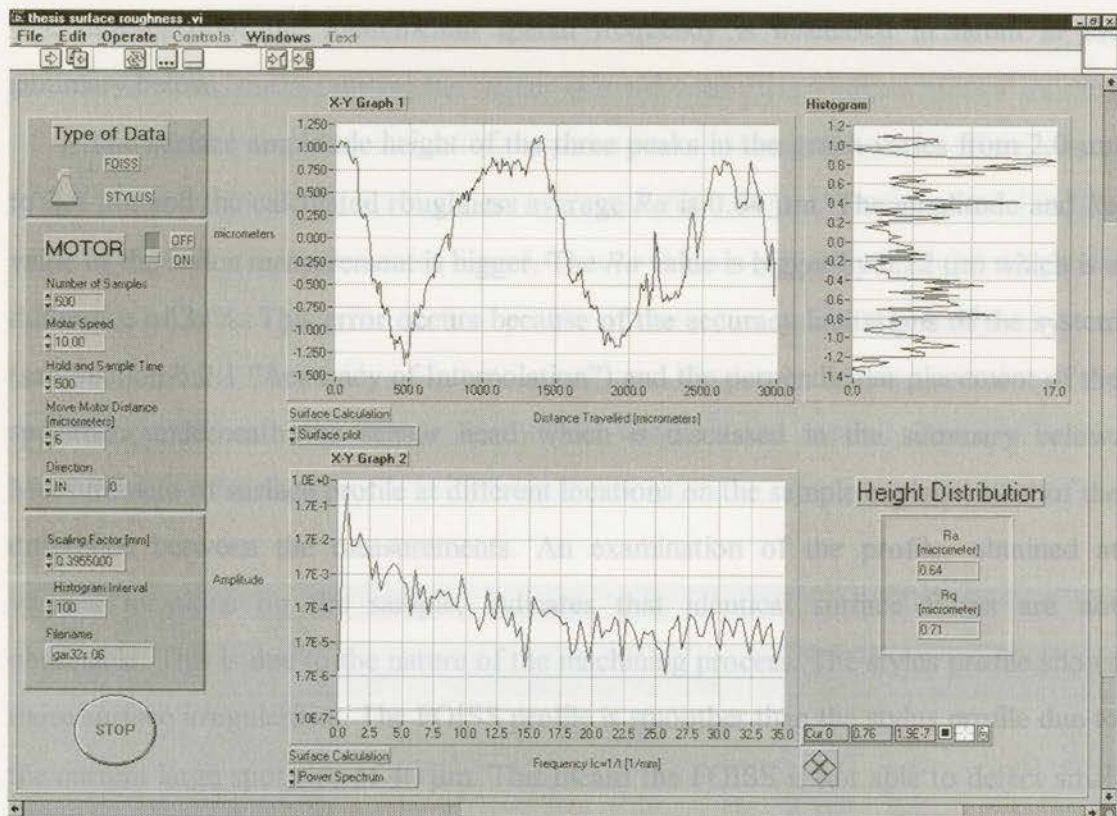


Figure 7.4: Mitutoyo measurement, Sample #1

The fundamental surface spatial frequency is 0.76 mm^{-1} , which corresponds to a 1.31 mm peak-to-peak distance. The measurement with the stylus indicates a wider spacing than the FOISS, which can be explained by the following two reasons: (1) The inaccuracy of the DC-motor translation stage system that positions the sample underneath the sensor head. The translation stage is moved against a spring which increases the motor load, with the result that the intended step is diminished. (2) The inaccuracies caused by a large laser spot size. The theory of the interferometer assumes that the strongest signal is the light reflected back from the center of the spot. If, for example, there is a strong reflection back into the probe from the edge of the spot, that swamps the signal from the center, the measurement will be referenced to the edge. This problem may be overcome by making the spot size smaller. Light reflected from different locations within the spot changes the measurement and the spatial parameter.

The difference of the fundamental spatial frequency is discussed in detail in the summary below. The surface amplitude height of the three peaks in the graph varies from $2.0\ \mu\text{m}$ to $2.4\ \mu\text{m}$ and the calculated roughness average Ra is $0.64\ \mu\text{m}$. The amplitude and Ra value of the stylus measurement is bigger. The Ra value is bigger by $0.22\ \mu\text{m}$ which is a difference of 34%. This error occurs because of the accuracy limitations of the system (see Section 6.2.1 "Accuracy of Interpolation") and the perpendicular placement of the specimen underneath the sensor head which is discussed in the summary below. Measurement of surface profile at different locations on the sample explains most of the difference between the measurements. An examination of the profile, obtained at various locations on the sample, indicates that identical surface forms are not obtainable. This is due to the nature of the machining process. The stylus profile shows more surface irregularities. The FOISS profile is smoother than the stylus profile due to the current large spot size of $40\ \mu\text{m}$. This means the FOISS is not able to detect small irregularities spaced less than $40\ \mu\text{m}$ apart. The histogram shows that the positive values dominate, which is due to the width of the peaks and indicates valleys.

Factors influencing accuracy will be discussed in more detail in the summary of the comparison at the end of this chapter.

Sample #2

Sample #2 is created by a horizontal milling process. Visual inspection of the surface shows it is more reflective than the shaped sample #1. Examining the surface more closely reveals the feed marks from the milling process, and by running a fingernail over the surface the lay marks can be felt.

The results for the FOISS measurements on sample #2 are shown in Figure 7.5. Inspection of the surface and examination of the power spectrum show a fundamental frequency of $1.0\ \text{mm}^{-1}$ and a corresponding $1.00\ \text{mm}$ peak-to-peak distance. The peaks correspond to the feed marks. Visual inspection of the surface profile shows the

occurrence of the peaks is due to the direction of cutting with the mill cutter. Chips are pulled out of the surface during the milling process, when the feedrate and the rotation of spindle direction are the same. This explains the width and steepness of the peaks, which occur very suddenly and have some irregularities on the top of the peak [2]. The amplitude of the four peaks varies from $1.0\ \mu\text{m}$ to $2.2\ \mu\text{m}$ and the calculated roughness average (R_a) is $0.49\ \mu\text{m}$. The surface profile waviness has small irregularities in it and the peak tops are steep with irregularities on them. The histogram shows a clear trend to the negative values which is due to the width of the valleys. This shows the asymmetrical surface profile. It has an abundance of peaks.

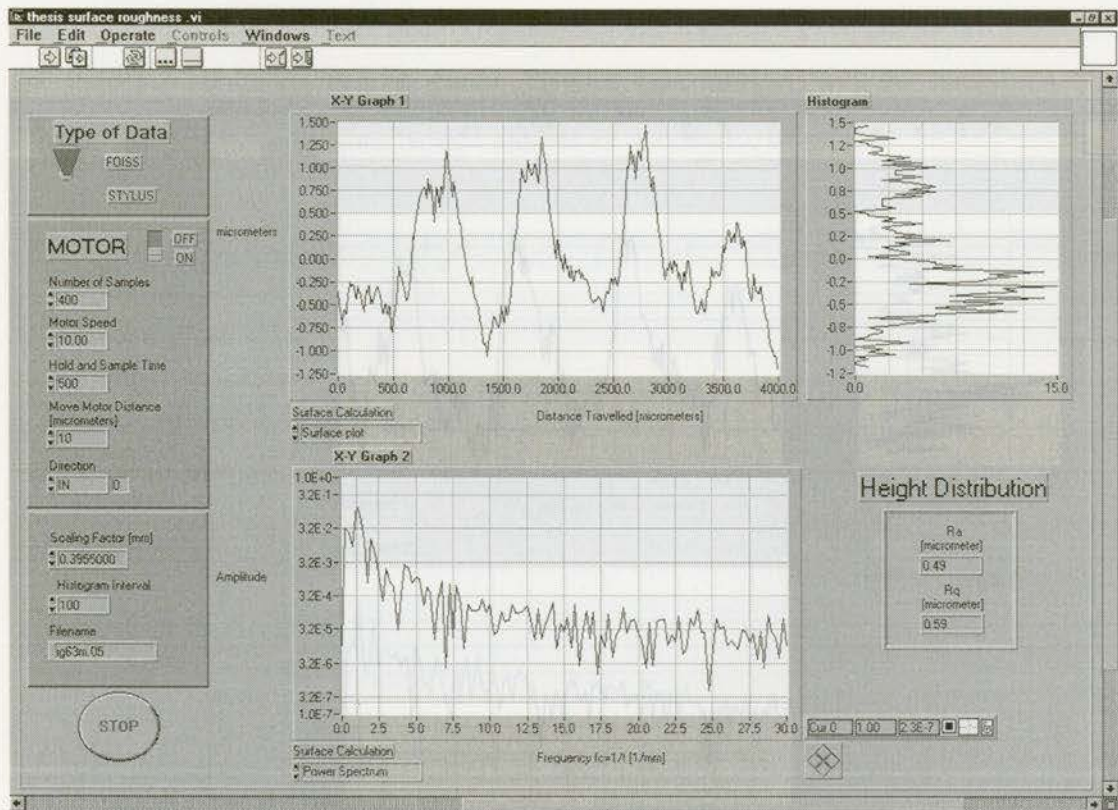


Figure 7.5: FOISS measurement, Sample #2

Figure 7.6: Mitutoyo measurement, Sample #2

Figure 7.6 shows the second surface sample measured with the Mitutoyo. The power spectrum graph shows a fundamental frequency of $0.95\ \text{mm}^{-1}$, which

corresponds to 1.05 mm peak-to-peak distance. This corresponds with both the FOISS measurement and the visual inspection of the surface. The amplitude of the four peaks varies from 2.0 μm to 3.0 μm and the calculated roughness average (R_a) is 0.68 μm . The R_a value of the stylus measurement is bigger by 0.19 μm which means a difference of 27%. The surface peaks are steep and have a few irregularities on the peaks tops. The valleys show more variations and irregularities than the tops. The FOISS profile is smoother than the stylus profile. The difference can again be explained by the measurement of different locations on the surface sample with both measuring methods and by the dimension of the laser spot size, which is discussed in the summary at the end of this Chapter.

to 4.5 μm . The calculated roughness average (R_a) is 0.97 μm . The surface profile waviness has small irregularities superimposed, the peaks are sharp and the valleys are smoother than the peaks. This can be confirmed with the histogram. The

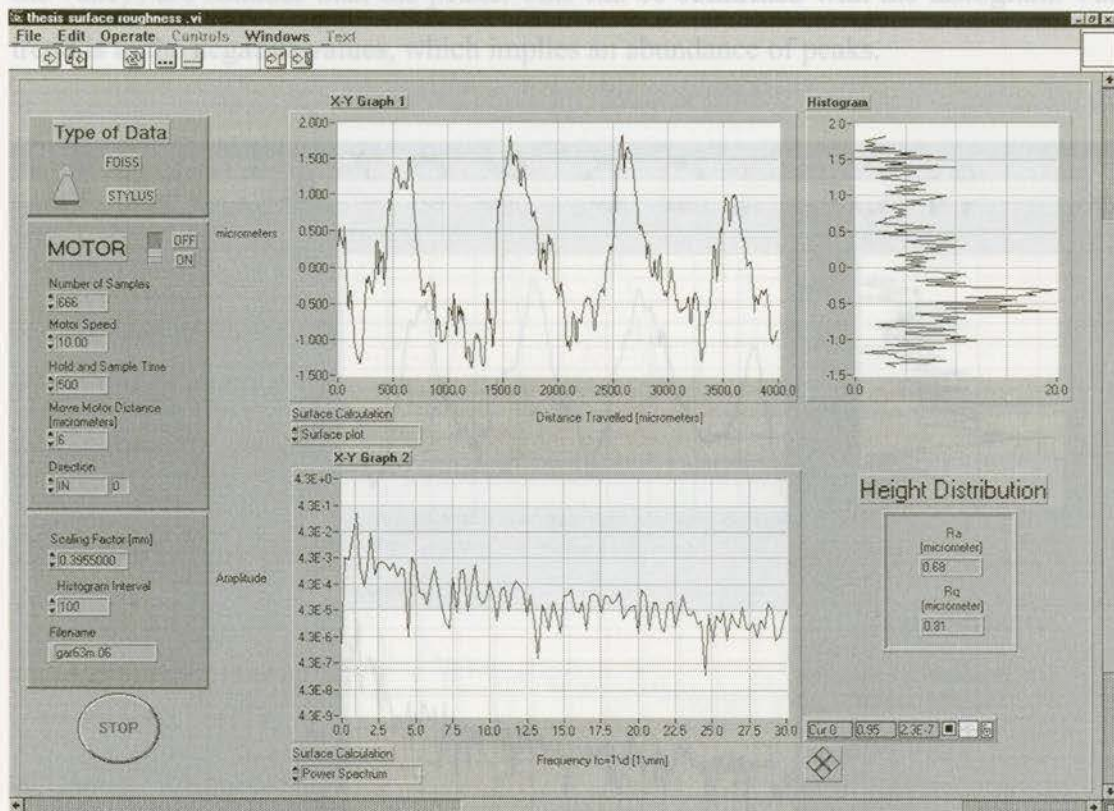


Figure 7.6: Mitutoyo measurement, Sample #2

Figure 7.7: FOISS measurement, Sample #3

Sample #3

The third surface sample represents a rougher horizontal milling process. Visual inspection of the surface shows a reflective surface with visible lay marks. The lay marks create a shadow pattern on the surface if the light strikes the sample correctly. Running a fingernail over the surface confirms the presence of the lay marks.

Figure 7.7 shows the FOISS results. The power spectrum graph displays a fundamental frequency of 0.80 mm^{-1} , which corresponds to a 1.25 mm separation of the lay marks. Visual inspection of the surface profile shows four peaks and the amplitude varies from $3.0 \text{ }\mu\text{m}$ to $4.5 \text{ }\mu\text{m}$. The calculated roughness average (R_a) is $0.97 \text{ }\mu\text{m}$. The surface profile waviness has small irregularities superimposed, the peaks are sharp and the valleys are rounder than the peaks. This can be confirmed with the histogram. The trend is to the negative values, which implies an abundance of peaks.

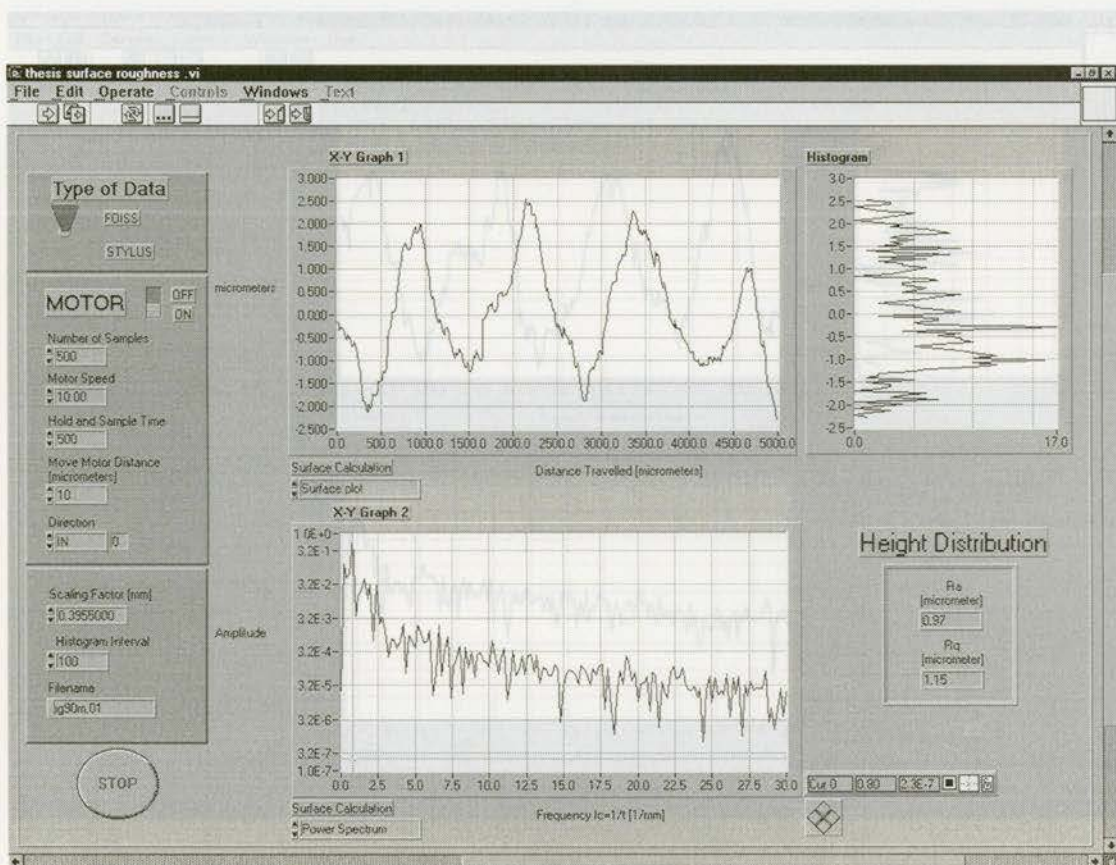


Figure 7.7: FOISS measurement, Sample #3

Figure 7.8 shows the third surface sample measured with the Mitutoyo stylus. Inspecting the measured profiles shows good similarities. From the power spectrum graph, the fundamental frequency of 0.80 mm^{-1} is measured, which corresponds to a 1.25 mm lay mark distance. This values obtained from the FOISS fundamental frequency match each other within the experimental error. The errors are discussed later in the summary. The amplitude of the four peaks vary from $5.0 \mu\text{m}$ to $5.5 \mu\text{m}$ and the calculated roughness average (R_a) is $0.97 \mu\text{m}$. The R_a value of the stylus measurement is bigger by $0.4 \mu\text{m}$ which is a difference of 29%. This error is again related to the accuracy limitation of the FOISS. There are more surface irregularities and they are stronger than those detected by the FOISS. The stylus picks up more detail because of the known limitation of the FOISS spot size. The histogram shows the same in both graphs, an abundance of peaks.

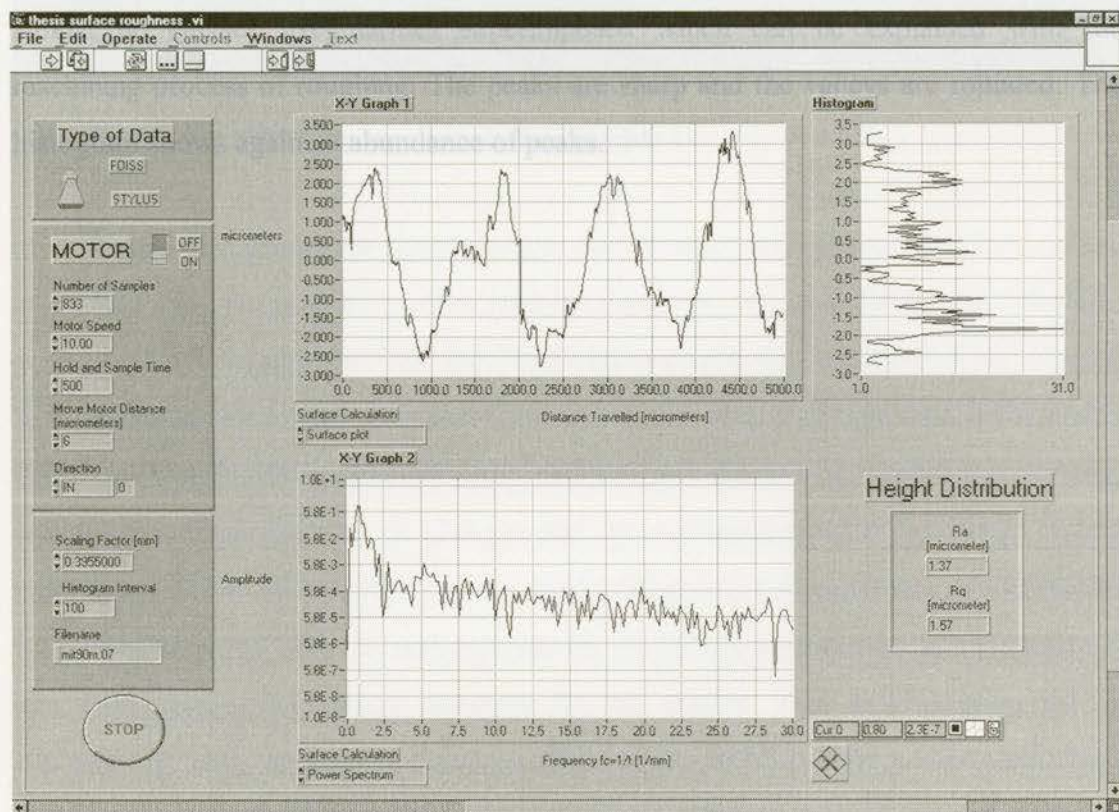


Figure 7.8: Mitutoyo measurement, Sample #3

Sample #4

Finally, the roughest surface, Sample #4, is measured. It represents a horizontal milling process with a high feed rate, as in a roughing process employed to get a workpiece to its rough dimensions with the intention of performing a finishing cut at a later date. The sample shows very strong lay marks. It is reflective and the marks are widely spaced. Crudely measured with a ruler, the spacing is about 2 mm.

Figure 7.9 shows the fourth sample surface measured with the FOISS. From the power spectrum graph a fundamental frequency of 0.51 mm^{-1} is found, which corresponds to a 1.96 mm peak-to-peak distance. This is exactly what was expected from visual inspection and the measurement with a ruler of the surface, widely spaced feed rate marks. The amplitude of the four peaks varies from $10.0 \text{ }\mu\text{m}$ to $11.0 \text{ }\mu\text{m}$ and the calculated roughness average R_a is $2.89 \text{ }\mu\text{m}$. The surface profile waviness has almost no surface irregularities superimposed which can be explained with the machining process of roughing. The peaks are sharp and the valleys are rounded. The histogram shows again an abundance of peaks.

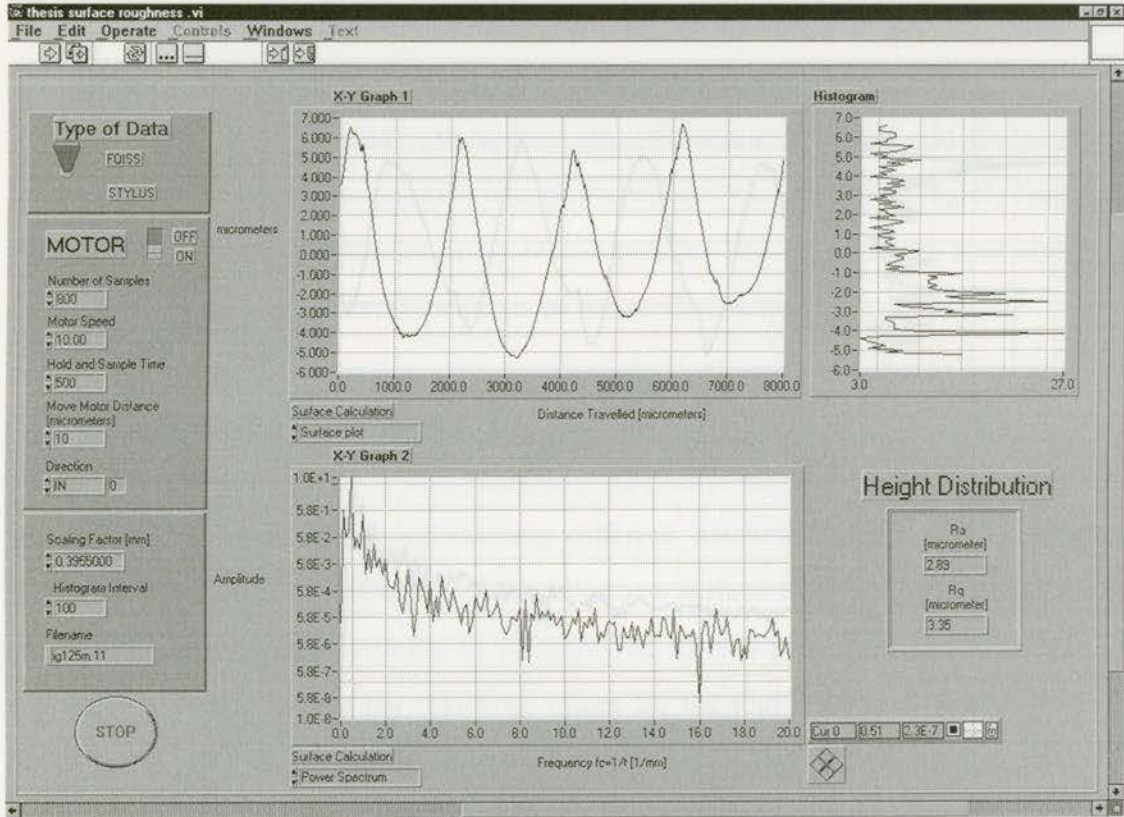


Figure 7.9: FOISS measurement, Sample #4

Figure 7.10 shows the fourth surface sample measured with the Mitutoyo stylus. A comparison of the surface profiles reveals similarities, however they are not identical. A fundamental frequency of 0.50 mm^{-1} was obtained with the stylus, which corresponds to a 2.0 mm peak-to-peak distance. This corresponds very well with the FOISS profile and represents the existence of 50 feed marks in both cases. The amplitude of the four peaks varies from $10.0 \text{ }\mu\text{m}$ to $12.0 \text{ }\mu\text{m}$ and the calculated roughness average is $3.50 \text{ }\mu\text{m}$. The R_a value of the stylus measurement is bigger by $0.61 \text{ }\mu\text{m}$ which can be related to a difference of 17.5%. In each sample, the R_a values as measured by the Mitutoyo are ~20% larger than those measured by the FOISS. This inconsistency will be discussed in more detail in the summary. The surface profile has sharp peaks and only a few irregularities on the waviness. On the stylus profile the bottom are narrower and have a small bump before the bottom on the negative slope. The FOISS profile is

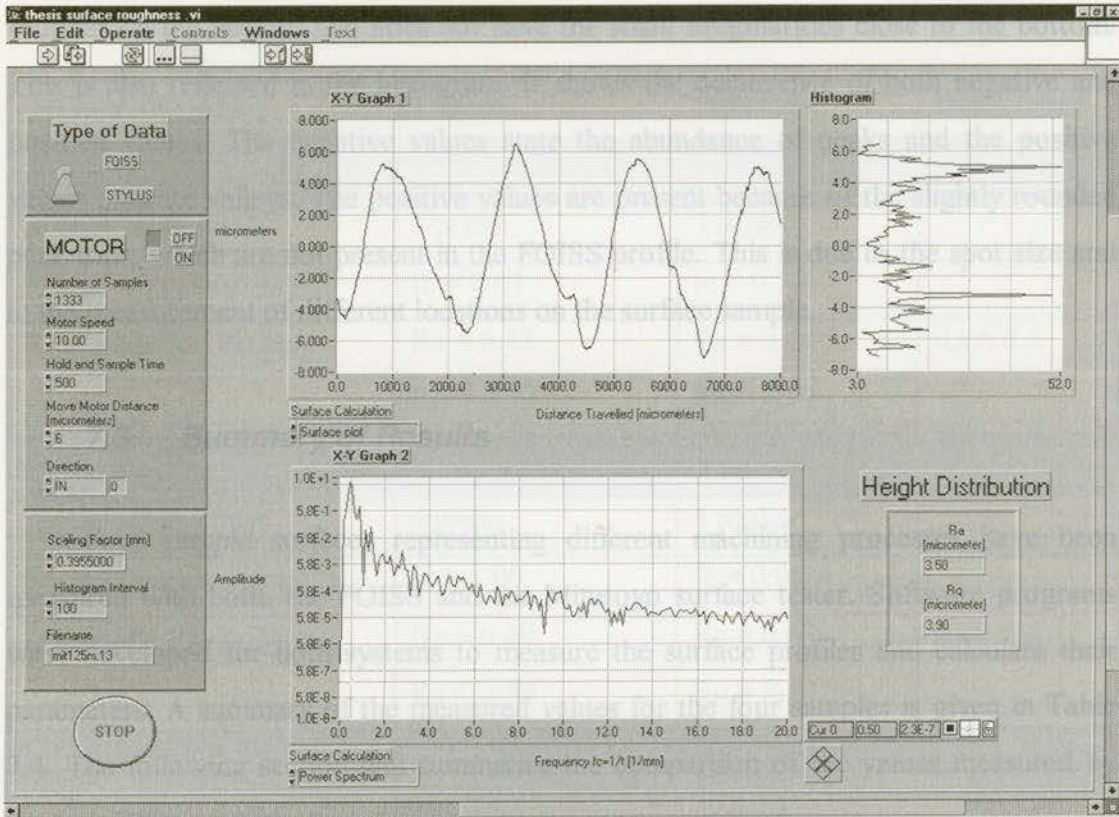


Figure 7.10: Mitutoyo measurement, Sample #4

Figure 7.10 shows the fourth surface sample measured with the Mitutoyo stylus. A comparison of the surface profiles reveals similarities, however they are not identical. A fundamental frequency of 0.50 mm^{-1} was obtained with the stylus, which corresponds to a 2.0 mm peak-to-peak distance. This corresponds very well with the FOISS profile and represents the existence of the feed marks in both cases. The amplitude of the four peaks varies from $10.0 \text{ }\mu\text{m}$ to $12.0 \text{ }\mu\text{m}$ and the calculated roughness average is $3.50 \text{ }\mu\text{m}$. The R_a value of the stylus measurement is bigger by $0.61 \text{ }\mu\text{m}$ which can be related to a difference of 17.5%. In each sample, the R_a values as measured by the Mitutoyo are $\sim 20\%$ larger than those measured by the FOISS. This inconsistency will be discussed in more detail in the summary. The surface profile has sharp peaks and only a few irregularities on the waviness. On the stylus profile the bottom are narrower and have a small bump before the bottom on the negative slope. The FOISS profile is

rounder on the bottom and does not have the small irregularities close to the bottom. This is also reflected in the histogram. It shows the occurrence of both negative and positive values. The negative values state the abundance of peaks and the positive values indicate valleys. The positive values are present because of the slightly rounded peak tops, which are not present in the FOISS profile. This is due to the spot size and to the measurement of different locations on the surface sample.

7.3. Summary of Results

Four sample surfaces representing different machining processes have been measured with both, the FOISS and the Mitutoyo surface tester. Software programs were developed for both systems to measure the surface profiles and calculate their parameters. A summary of the measured values for the four samples is given in Table 7.4. The following section will summarize the comparison of the values measured by the two different methods:

- The number of spatial peaks has been found to be consistent throughout the comparison for both measurements and for all samples in the Ra range $0.42 \mu\text{m} \leq Ra \leq 2.89 \mu\text{m}$.
- The spatial frequency also matches well except for the first measured sample. Here, the translation stage error and the random surface error account for the differences.
- The amplitude, Ra and Rq , consistently disagrees with the measurement of the stylus. The difference of the Ra value measured by the FOISS and by the stylus is between 17% and 34%. This leads to the conclusion that there is a systematic error in the system. The variations will be explained next with a focus on spot size error and calibration error.
- Visual inspection of both measurements show similar profiles. The irregularities that are more visible on the stylus profile can be explained with the spot size error.

Table 7.4: Comparison of measured data

Surface Property	FOISS	Mitutoyo	Dial Gauge
<i>Surface Sample #1, Shaped</i>			
Spatial, peak count	3 peaks	3 peaks	
Spatial frequency (mm^{-1})	$f_c = 0.87$	$f_c = 0.76$	
Amplitude R_a , R_q (μm)	$R_a = 0.42$ $R_q = 0.52$	$R_a = 0.64$ $R_q = 0.71$	$R_a = 0.6$
<i>Surface Sample #2, Milled</i>			
Spatial, peak count	4 peaks	4 peaks	
Spatial frequency (mm^{-1})	$f_c = 1.00$	$f_c = 0.95$	
Amplitude R_a , R_q (μm)	$R_a = 0.49$ $R_q = 0.59$	$R_a = 0.68$ $R_q = 0.81$	$R_a = 0.6$
<i>Surface Sample #3, Milled</i>			
Spatial, peak count	4 peaks	4 peaks	
Spatial frequency (mm^{-1})	$f_c = 0.80$	$f_c = 0.80$	
Amplitude R_a , R_q (μm)	$R_a = 0.97$ $R_q = 1.15$	$R_a = 1.37$ $R_q = 1.57$	$R_a = 1.4$
<i>Surface Sample #4, Milled</i>			
Spatial, peak count	4 peaks	4 peaks	
Spatial frequency (mm^{-1})	$f_c = 0.51$	$f_c = 0.50$	
Amplitude R_a , R_q (μm)	$R_a = 2.89$ $R_q = 3.35$	$R_a = 3.50$ $R_q = 3.90$	$R_a = 3.4$

The discrepancies in the measurement between the FOISS and stylus parameters can be explained by: translation stage error, calibration error, spot size error, and random surface error. The error of $\pm 0.007 \mu\text{m}$ would be very small, but with the FOISS this is not the case. The problem lies in the position of the surface to the probe head. This problem is also addressed by Stedman [3]. As mentioned before, the

1. Translation Stage Error

The measured spatial frequency can appear to change because of the DC motor used for positioning the stage with the surface sample underneath the sensor head. It is not a servo system but an open-loop system. The stage is pulled against the motor through a spring and held in position by this mechanism. Moving the translation stage out, or against the spring, changes the load of the motor because as the spring extends the force required increases. The DC motor is operated by sending a voltage level for a certain time to it. With the load increasing, and the time interval to move the motor one step staying the same, then the distance traveled per step decreases. This error only occurs when the motor is moved against the spring. In the first measurement it can be seen on the front panel that the direction of the motor was "out", hence against the spring. Measurements with a clock dial have shown that moving inwards is more accurate. After this error had been detected it was solved by making all other measurements of the samples while moving the motor inwards which eliminates the problem.

2. Calibration Error

One component of the amplitude height variation between the FOISS and the stylus occurs because of the overall accuracy of the FOISS. In Section 7.2.1, the accuracy of the system has been proven to be $\pm 0.007 \mu\text{m}$ for a move of one fringe on the MI ($0.3164 \mu\text{m}$). This means for every $0.3164 \mu\text{m}$ moved relative to the FOISS the error is $\pm 0.007 \mu\text{m}$. The problem is that the error accumulates over large distances. Looking at the measured profiles, let us assume that the error can be neglected because the maximum surface profile amplitude is only $12 \mu\text{m}$. This overall error would be about forty times $\pm 0.007 \mu\text{m}$. The error of $\pm 0.280 \mu\text{m}$ would be very small, but with the FOISS this is not the case. The problem lies in the position of the surface to the probe head. This problem is also addressed by Stedman [3]. As mentioned before, the

surface cannot be placed perfectly perpendicular underneath the sensor head as shown in Figure 7.11. The bottom graph shows the measurement as it was taken and the top graph shows the profile after the linear regression calculation. The surface has its reference at the first measured value, which is always zero. The rest of the data is measured with respect to zero and when the surface has an overall slope this gets measured as well. While recording the data, it was discovered that the overall distance measured often exceeds 100 μm . This does not get displayed in the front panel because the profile is “fixed” through the linear regression. The calculated best fit is used to translate the measured surface profile to its mean line. The 100 μm would give a false surface height of $\pm 2.2 \mu\text{m}$ in the worst case. This can partially account for the overall variation in R_a and R_q .

This error can be eliminated by adjusting the probe, or the surface, so they are perfectly perpendicular to each other.

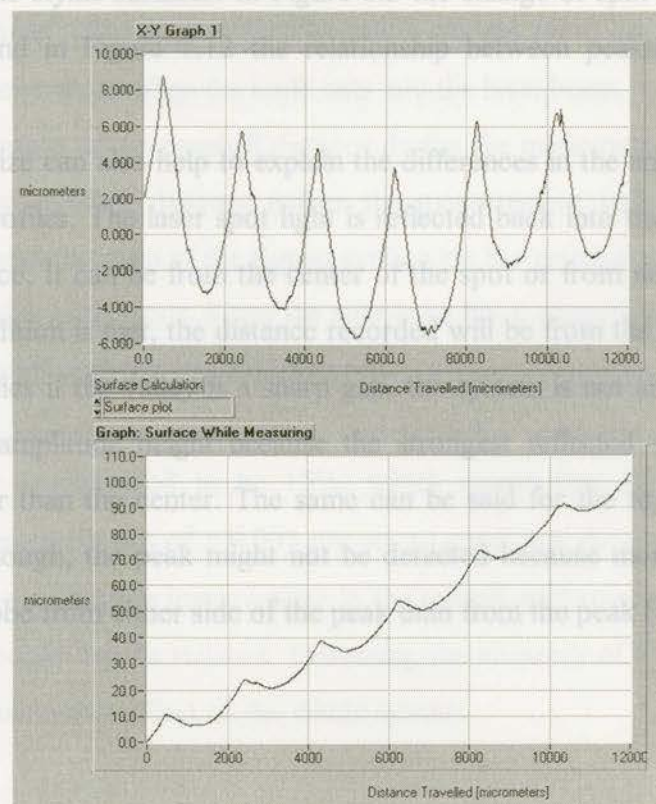


Figure 7.11: Calibration error

3. Error Due To Laser Spot Size

The spot size of the laser is the most critical and important factor of the FOISS. The standoff distance between the surface and the probe has to be very exact to maintain the same spot size. Since this is so critical, an effort was made to adjust the standoff distance with a vertical translation stage. However, after comparing the samples this seems not to be good enough. The adjustment of the standoff distance is critical. Changing the standoff distance by half a millimeter results in double the spot size. This means that the spot size can vary between 40 μm and 80 μm . Comparing these values with the standard stylus probe tip radius of 12 μm reveals why the surface profiles measured with the stylus have more detail than the FOISS measurement. Even when the spot size is at its minimum of 40 μm , the system misses detail of the surface that the stylus detects. This is why the surfaces measured with the FOISS look smoother than the stylus surfaces. In Figure 8.3 the change of spot size is shown on a round surface and in Figure 7.12 the relationship between peaks and laser spot is shown.

The spot size can also help to explain the differences in the amplitude value (Ra) of the surface profiles. The laser spot light is reflected back into the probe from some part of the surface. It can be from the center of the spot or from near the edge. If the interference condition is met, the distance recorded will be from the strongest reflected signal. This implies if the valley is a sharp gap, the system is not able to detect it and this affects the amplitude height because the strongest reflected signal occurs from either side rather than the center. The same can be said for the tops of peaks. If the peak is sharp enough, the peak might not be detected because more light is reflected back into the probe from either side of the peak than from the peak (see Figure 7.12).

laser spot size should first be reduced. Increasing the accuracy of the interpolation will not have any considerable affect on the whole system.

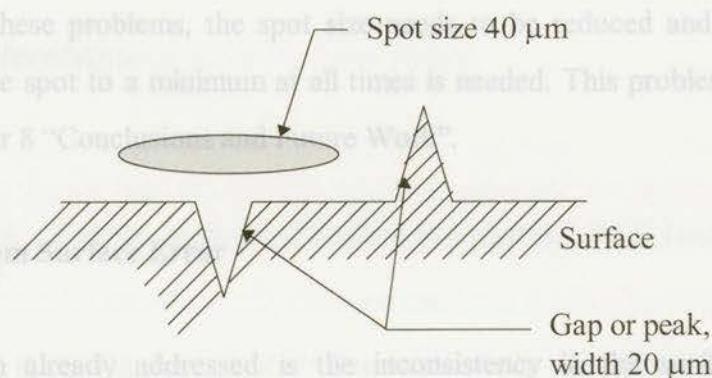


Figure 7.12: Spot size in comparison to surface

It was found that the spot size error is the biggest source of inaccuracy in the system. The spot size error includes the following.

- 1) The error of measuring the spot size. As explained in Section 4.2 “Calculation of Laser Spot Size”, this error is mostly due to human error. In the experiment the human eye determines when the knife cuts into the laser beam.
- 2) The error because of the standoff distance during the measurement. The inaccuracy of setting the standoff distance before the measurement and the change of the standoff distance because of the sloped surface are the prime sources of this error.
- 3) The overall size of the spot. Since the spot is so big it changes considerably during the measurement with the standoff distance.

This error is estimated to be 15%, which means that other errors like the accuracy of the interpolation of $\pm 0.007 \mu\text{m}$ are so small that they can be neglected. In order to achieve a noticeable improvement in the overall performance of the system the laser spot size should first be reduced. Increasing the accuracy of the interpolation will not have any considerable effect on the whole system.

To solve these problems, the spot size needs to be reduced and a mechanism which focuses the spot to a minimum at all times is needed. This problem is discussed further in Chapter 8 "Conclusions and Future Work".

4. Random Surface Error

A problem already addressed is the inconsistency in the surface profile at different locations. A machining process incorporates many parameters, so surface profiles taken at different locations on the sample are not identical. After the surface sample was measured with the FOISS it had to be moved and repositioned for the stylus measurement. Measuring different locations on the sample will give different profiles. This makes profile comparisons less objective and more subjective.

It has been found during the measurements that smoother samples have a more random surface profile than rougher samples. The visual inspection of the first measured profile by the FOISS does not show a very similar pattern with itself. The same is true for the stylus measurement. The profiles for a smooth surface are not as consistent as the rougher milled samples because there are no distinct lay marks. Depending on the type of tool that has been used and the condition of the tool (due to tool wear) the surface at different locations of the same sample will look different.

This problem has been found with other smooth samples as well. For the evaluation of the FOISS rougher samples are more appropriate because the errors that are present can be better identified and later eliminated.

A surface sample with a known profile, e.g. sinusoidal over the whole sample, would have been very helpful for the evaluation of the FOISS. Such perfect standard samples are not available.

7.4. References and Future Work

[1] Michael Brock, "Fourier Analysis of Surface Roughness," *B&K Technical Review*, no. 3, 1983: 3-45.

[2] Beit, W. And K.-H. Küttner, *Dubbel: Taschenbuch für den Maschinenbau*, Berlin: Springer Verlag, 1987.

[3] Margaret Stedman, "Limits of Surface Measurement by Optical Probes," *SPIE, Surface Measurement and Characterization*, vol. 1009, 1988: 62-67.

Four different surface samples have been recorded through the software for both the FOISS and the Mitutoyo stylus. Each profile was carefully compared and discussed. The FOISS has a vertical measuring resolution of $\pm 0.007 \mu\text{m}$ over one fringe, which is better in comparison to the Mitutoyo stylus of $0.02 \mu\text{m}$. However, limitations in the resolution were found which are due in decreasing order to:

- 1) error due to spot size,
- 2) calibration error,
- 3) random surface error, and
- 4) translation stage error.

At this stage, the system is not suitable for industrial development because of its obvious limitations. As shown in the work, the system has the ability to measure surface profiles. It was successfully changed from a pressure measuring device to a non-contact surface roughness measuring instrument. Further changes to the system will increase its precision and accuracy. Potential improvements to the FOISS are discussed below.

8. Conclusions and Future Work

It has been shown that the FOISS, originally intended for pressure sensing via precise diaphragm deflection measurement, is able to measure surface roughness. The FOISS was theoretically examined and different methods for the conversion from volts to microns were examined. A method for the calibration of the FOISS was developed and the laser spot size was calculated and measured to determine the accuracy of the system. Software was developed first to calibrate the FOISS and then to read and analyze measured data. An industry-standard stylus surface tester was used for comparison with the measured data from the FOISS. The stylus was only able to display the R_a value on a dial gage, but to overcome this problem a software module was developed that can read and process the stylus data.

Four different surface samples have been recorded through the software for both the FOISS and the Mitutoyo stylus. Each profile was carefully compared and discussed. The FOISS has a vertical measuring resolution of $\pm 0.007 \mu\text{m}$ over one fringe, which is better in comparison to the Mitutoyo stylus of $0.02 \mu\text{m}$. However, limitations in the resolution were found which are due in decreasing order to:

- 1) error due to spot size,
- 2) calibration error,
- 3) random surface error, and
- 4) translation stage error.

At this stage, the system is not suitable for industrial development because of its obvious limitations. As shown in the work, the system has the ability to measure surface profiles. It was successfully changed from a pressure measuring device to a non-contact surface roughness measuring instrument. Further changes to the system will increase its precision and accuracy. Potential improvements to the FOISS are discussed below.

8.1. Future Work

The main problem in the work with the FOISS was found to be the laser spot size and the focusing mechanism. The following suggestions will help eliminate these problems.

8.1.1. Reducing Laser Spot Size

There are different ways to reduce the laser spot size. One way would be to use a microscope objective to focus the spot. The disadvantage of this method is the loss of power because the light has to travel through long distances in air. Alternatively, a new probe setup could be constructed that is similar to the previous probe but with the difference that the fibre is not directly attached to the GRIN lens. The standoff distance for the focus of the spot decreases and so does the laser spot size.

A new probe was built and the gap between the GRIN lens and the fibre is about 0.3 mm. In a knife edge experiment the new spot size was measured at varying distances from the GRIN lens. The results are illustrated in Figure 8.1. The smallest spot size that was measured was 15 μm at a distance of 4 mm from the end of the Grin lens. Using a probe of this nature would greatly increase the resolution of the surface measurement. However, as shown in the graph, if the standoff distance varies by ± 0.5 mm, the spot size doubles and the initial advantage of a smaller spot is lost.

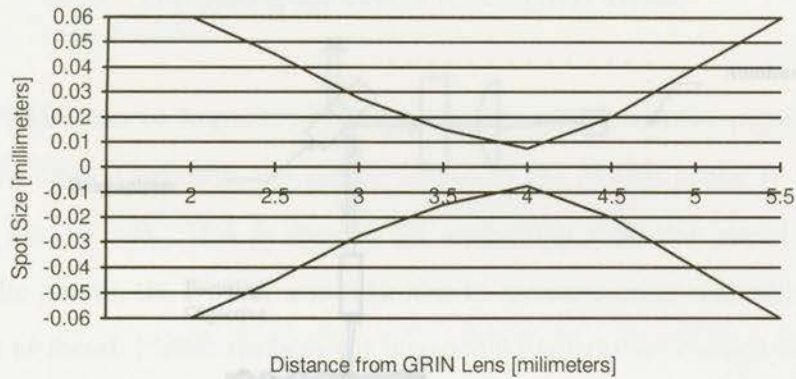


Figure 8.1: Laser spot size characteristics

The new probe cannot solve the problem with the exact positioning of the probe in relation to the surface sample and there is no considerable increase of accuracy in the system. For a more accurate system an autofocus method is needed, as shown next.

8.1.2. Autofocus Method

As the height of the surface changes, the spot size of the laser beam also changes. To eliminate the varying spot size when, the surface changes, an autofocus method must be used. Different autofocus methods have been developed and can be found in various papers [1, 2, 3]. The principle of an autofocus system by Bistow et al. [4] is shown in Figure 8.2. In Figure 8.3, the change in spot size with the change of the surface is demonstrated.

collimation of the reflected light. If the system is at best focus, the light will be collimated. A closed-loop servo is used to control the focal position of the objective to ensure a constant spot size.

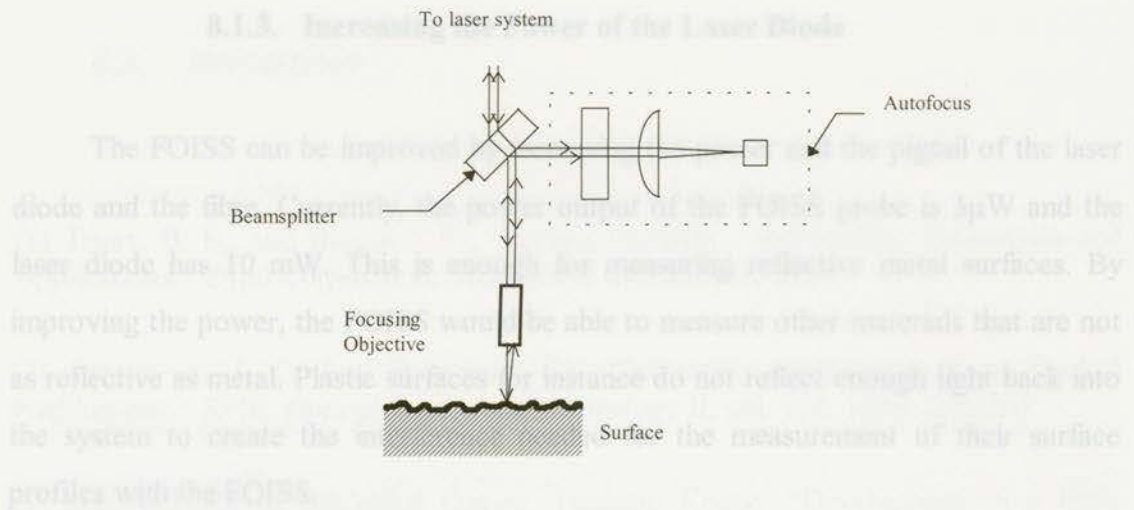


Figure 8.2: Autofocus method

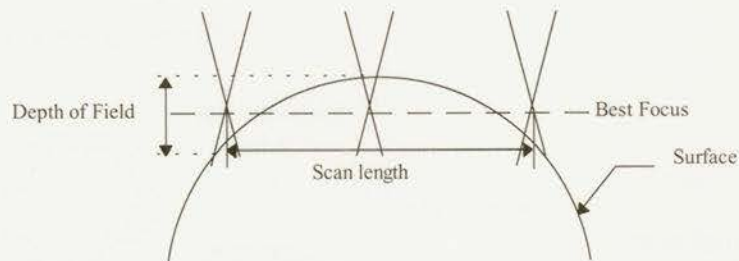


Figure 8.3: Spot size limitation

The light reflected from the sample passes back through the focusing objective to a beamsplitter into the autofocus system. A small amount of light (5%-10%) is reflected from the beamsplitter to the autofocus system. The autofocus system measures the degree of collimation of the reflected light. If the system is at best focus, the light will be collimated. A closed-loop servo is used to control the focal position of the objective to ensure a constant spot size.

8.2. References

- [1] Truax, B. E., and Biegen J. F., "Surface Profiling - Instruments, Techniques and Applications," Zygo Corporation, Middlefield Connecticut, USA.
- [2] Brown, A. J. C. And Breitmeier, U., "Industrial Applications of an Optical Profilometer," *SPIE, Optical Testing and Metrology II*, vol. 954, 1988: 200-207.
- [3] Kimiyuki Mitsui, Norimitsu Ozawa, Tusuguo Kohno, "Development of a High Resolution In-Process Sensor for Surface Roughness by Laser Beam", *Bulletin of the Japan Society of Precision Engineering*, vol. 19, no. 2, June 1985.
- [4] T.C. Bristow, G. Wagner, J.R. Bietry and R.A. Auriemma. "Surface Characterization and Testing II" *SPIE*, vol. 1164, 1989.

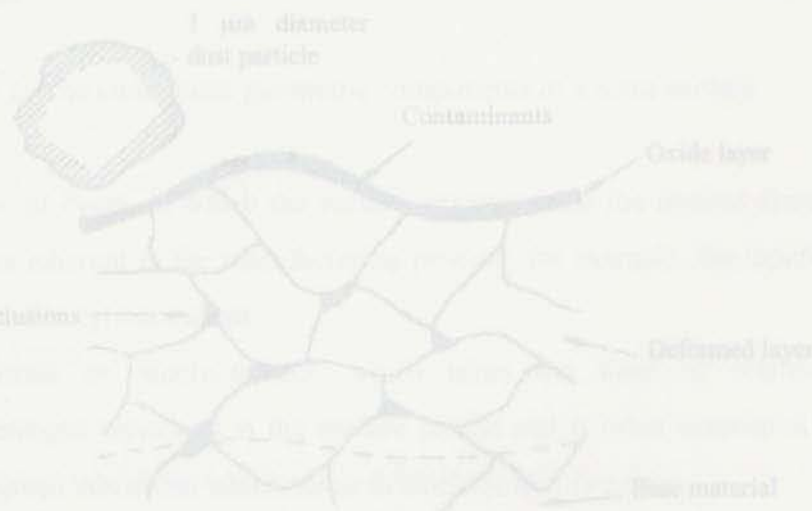


Figure 9.1: Typical surface layers

The geometric shapes of ordinary surfaces are controlled by the characteristics of the finishing processes by which they are produced. Close analysis of these surfaces

9. Appendix A

Nature of Metallic Surfaces and Surface Geometry

The surface of a typical metal is illustrated in Figure 1. On top of the normal crystalline structure of the bulk material lies a layer of deformed material resulting from the processes used in the manufacture of the surface. This deformed layer is itself covered by a compound layer resulting from chemical reaction of the metal with its environment. The reacted layer will, in a normal environment, often be covered with a layer of contaminants such as lubrication (oil), dust, and oxides. Machining processes may also have caused contaminants such as cutting lubricants to be trapped in heavily deformed regions of the surface [1].

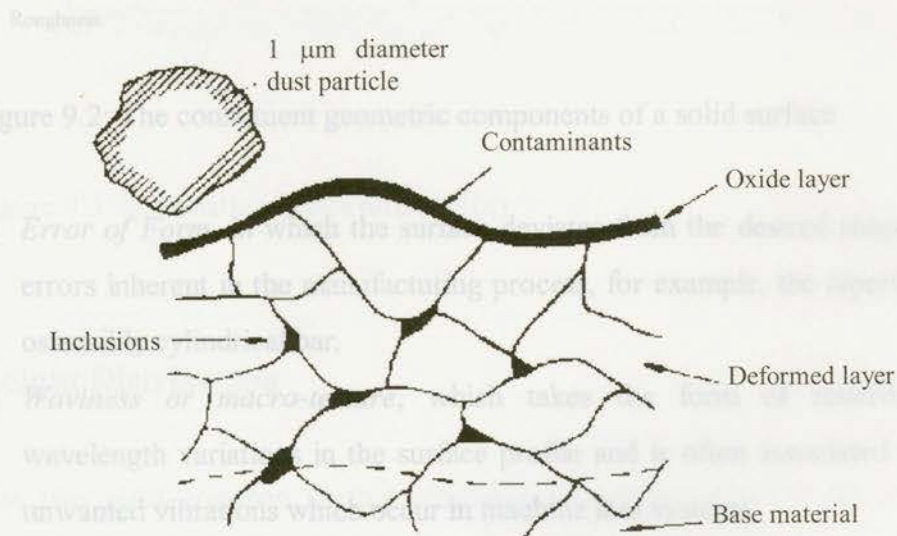


Figure 9.1: Typical surface layers

The geometric shapes of ordinary surfaces are controlled by the characteristics of the finishing processes by which they are produced. Close analysis of these surfaces

shows that, even after the most careful polishing, they are still rough on a microscopic scale. Statistical analysis of the undulations of a surface normally show that a very wide range of wavelengths is present, ranging from a fraction of a micrometer to many millimeters. It is likely that the range of wavelengths detected is limited only by the resolution of the measuring instrument and that the wavelength spectrum actually extends from atomic dimensions to the full length of the surface being measured. Surfaces are described using the ideas illustrated in Figure 2 and explained below.

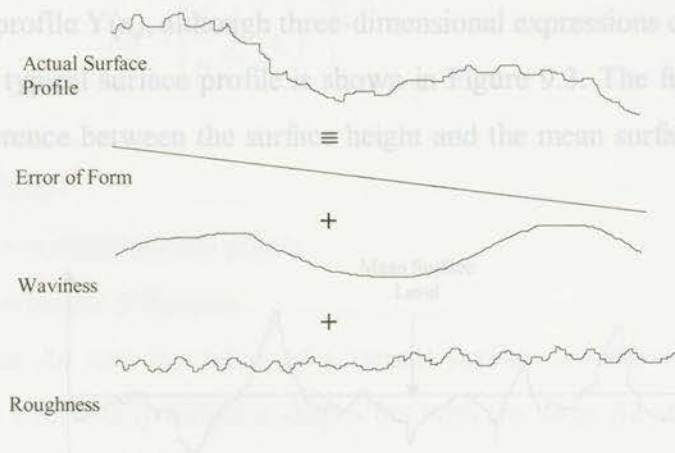


Figure 9.2: The constituent geometric components of a solid surface

- 1) *Error of Form*, in which the surface deviates from the desired shape due to errors inherent in the manufacturing process, for example, the tapering of an ostensibly cylindrical bar.
- 2) *Waviness or macro-texture*, which takes the form of relatively long wavelength variations in the surface profile and is often associated with the unwanted vibrations which occur in machine tool systems.
- 3) *Roughness or micro-texture*, which is the small-scale roughness of the surface associated with the actual cutting and/or polishing process during its production, e.g. by the action of the grits in abrasive processes. The peaks and valleys of the surfaces are also known as asperities. In tribology, for example, friction and wear both arise from the contacts between such asperities on opposing surfaces.

Statistical Analysis of Surface Profiles

To quantify the average properties of surface topography, a number of statistical functions and parameters have been developed [2]. These characterize the two basic aspects of topography: the heights of the asperities (amplitude) and the longitudinal spacing between the asperities (spatial period). Because surface profile samples are normally taken along a line, such parameters are defined in terms of a two-dimensional surface profile $Y(x)$, although three-dimensional expressions can also be used.

A typical surface profile is shown in Figure 9.3. The function $Y(x)$ is defined as the difference between the surface height and the mean surface level over the sampled line.

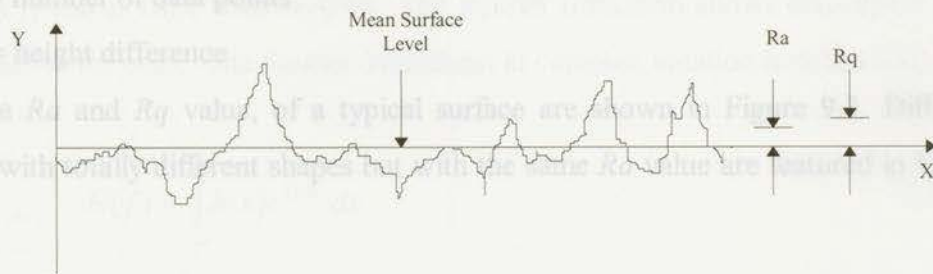


Figure 9.3: Schematic surface profile $Y(x)$

Height Distribution

The two most common surface roughness parameters are: (1) the roughness average (R_a) value, which is the mean vertical deviation of the profile from the center line, treating deviations both above and below the center line as positive; (2) the root mean square (RMS or R_q) value, defined as the square root of the mean of the square of these deviations. These parameters are only concerned with the relative departure from the center line in the vertical direction. They do not provide any information about shapes, slopes, and sizes of the asperities or about the frequency of their occurrence. It

is, therefore, possible for surfaces of widely different profiles to give the same Ra and Rq values [3]. These single-parameter descriptions are useful for comparing surfaces which have been produced to different standards but by similar methods.

Mathematically Ra and Rq are defined as:

$$Ra = \frac{1}{n} \sum_{i=1}^n |z_i| \tag{9.1}$$

$$Rq = \left[\frac{1}{n} \sum_{i=1}^n (z_i)^2 \right]^{\frac{1}{2}} \tag{9.2}$$

where

n = number of data points

z_i = height difference

The Ra and Rq value, of a typical surface are shown in Figure 9.3. Different surfaces with totally different shapes but with the same Ra value are featured in Figure 9.4 [4].

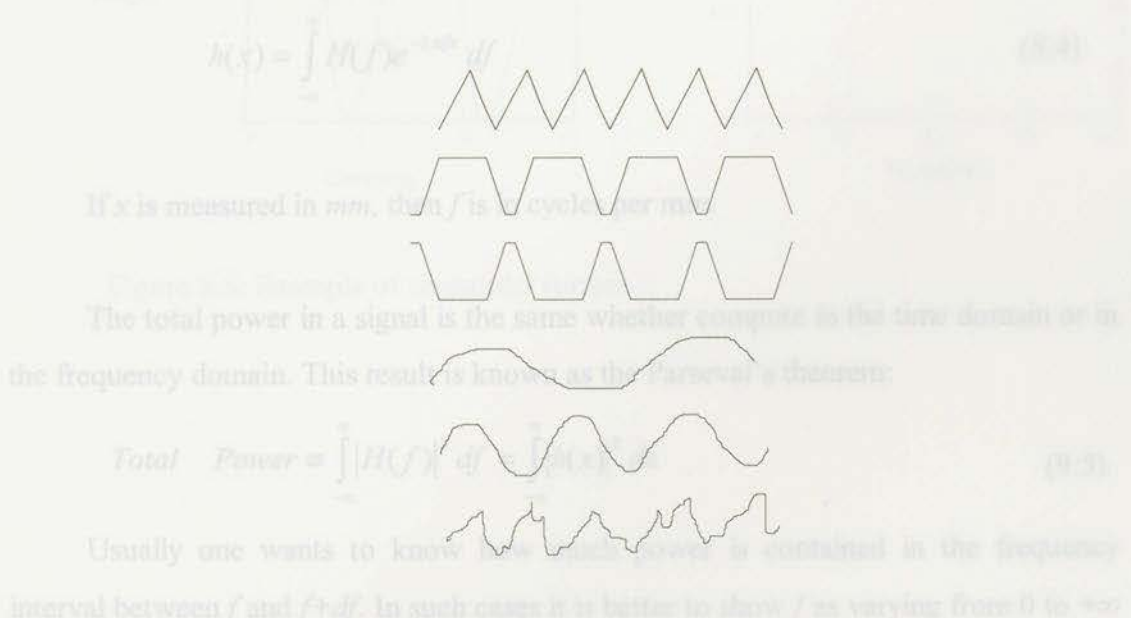


Figure 9.4: Geometric profiles having the same Ra values

(PSD) of the function h as

Surface Spatial Frequency

Surface profiles often reveal both periodic and random components in their geometric variation, and such components are not revealed by the statistical parameters like Ra and Rq values. The periodicity of the surface can be found with the power spectrum. The waviness of a surface can be examined in the frequency domain using the Fourier transform [5].

A physical process can be described either in the spatial domain, by the values of some quantity h as a function of distance x , that is $h(x)$, or else in the frequency domain, where the process is specified by giving its amplitude H as a function of frequency f , that is $H(f)$, with $-\infty < f < \infty$. The Fourier transform allows conversion from one domain to the other. The Fourier Transform in complex notation is defined as:

$$H(f) = \int_{-\infty}^{\infty} h(x) e^{2\pi i f x} dx \quad (9.3)$$

$$h(x) = \int_{-\infty}^{\infty} H(f) e^{-2\pi i f x} df \quad (9.4)$$

If x is measured in mm , then f is in cycles per mm .

The total power in a signal is the same whether compute in the time domain or in the frequency domain. This result is known as the Parseval's theorem:

$$\text{Total Power} \equiv \int_{-\infty}^{\infty} |H(f)|^2 df = \int_{-\infty}^{\infty} |h(x)|^2 dx \quad (9.5)$$

Usually one wants to know how much power is contained in the frequency interval between f and $f+df$. In such cases it is better to show f as varying from 0 to $+\infty$ and not from positive to negative f . This is called the one-sided power spectral density (PSD) of the function h as

$$Ph(x) \equiv |H(f)|^2 + |H(-f)|^2 \quad 0 \leq f \leq \infty \quad (9.6)$$

so that the total power is just the integral of $Ph(x)$ from $f=0$ to $f=\infty$. When the function $h(x)$ is real, then the two terms are equal, then

$$Ph(x) \equiv 2|H(f)|^2. \quad (9.7)$$

Surface spatial frequencies give information about height variations on the surface. A surface with a perfect sinusoidal profile will have one frequency component as shown in Figure 9.5. Real surfaces are obviously more complex and will have a lot more frequencies. By finding that the spectrum has a high amplitude at one frequency, it can be concluded that the surface has a periodicity. This often occurs when a part gets machined on a lathe with a high feedrate.

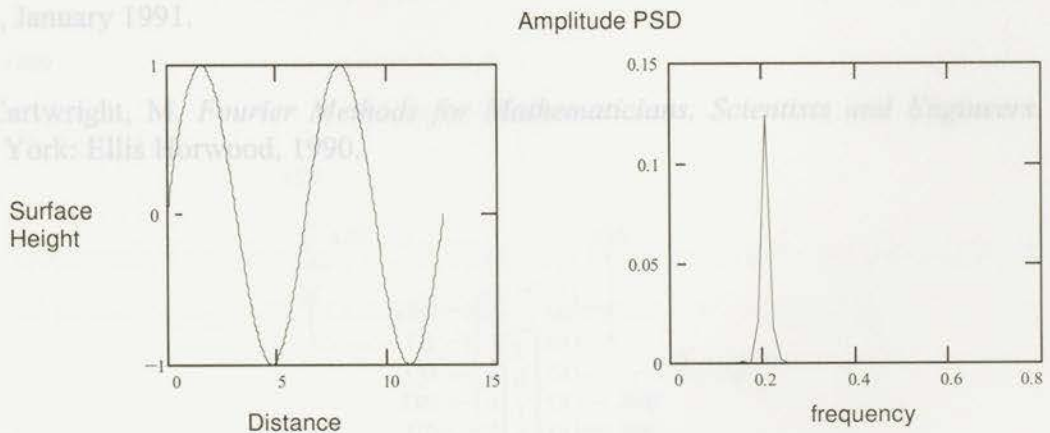


Figure 9.5: Example of sinusoidal surface

10. References

- [1] Arnell, R.D. *Tribology, Principles and Design Applications*. New York: Springer Verlag, 1991.
- [2] Vorburger, T.V. and Teague, E.C. "Optical Techniques for On-Line Measurement of Surface Topography" *Precision Engineering*, vol. 3, 1981: 61.
- [3] Dickson, M.S. and Harkness, D. "Surveying and Tracking Instruments" in R. Kingslake (ed.). *Applied Optics and Optical Engineering*, New York: Academic Press, vol. 5, 1969: 231.
- [4] Lovoie, R. A., "Understanding the Limits of Ra," *Manufacturing Engineering*, pp. 6, January 1991.
- [5] Cartwright, M. *Fourier Methods for Mathematicians, Scientists and Engineers*. New York: Ellis Horwood, 1990.

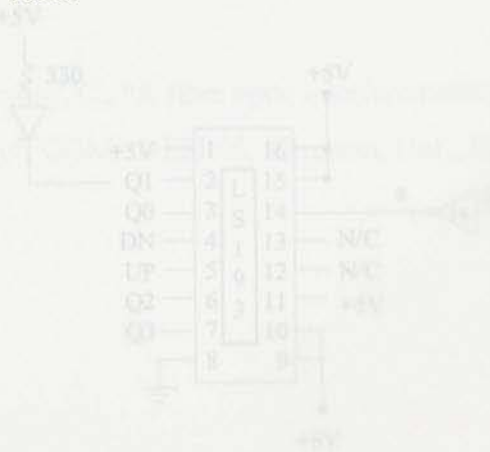
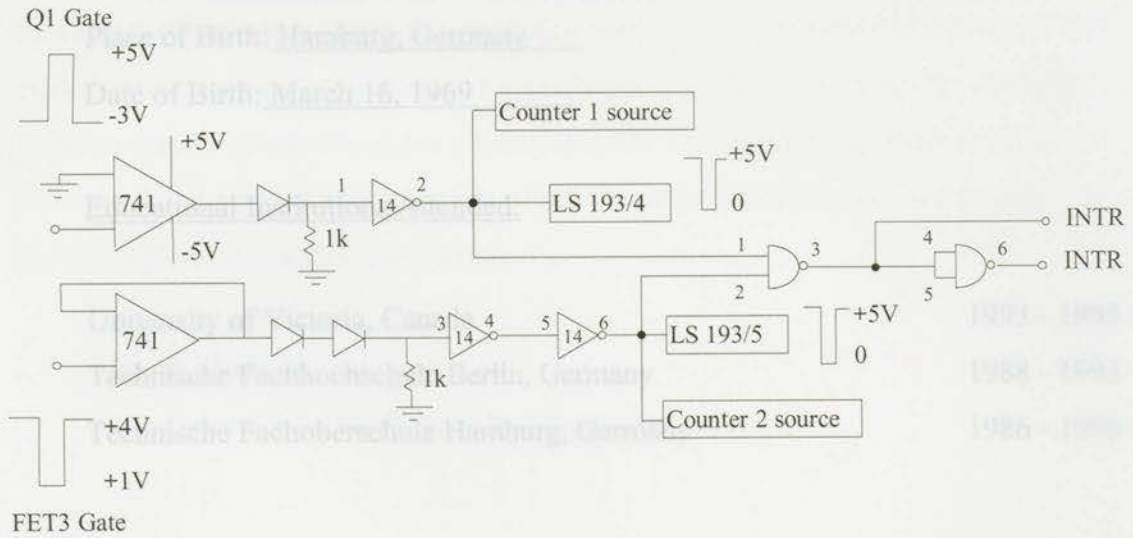


Figure 10.1: Schematic for digital card

10. Appendix B



Publications:

Bohmann, J. and Bräuer, G., "A fibre optic interferometer for the measurement of surface topography" *COMPTON JOURNAL*, Ont., June 1995.

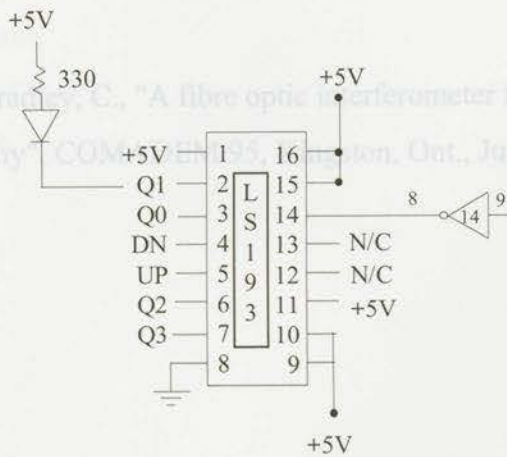


Figure 10.1: Schematic for digital card

VITA

Surname: Bohlmann Given Name: Jan

Place of Birth: Hamburg, Germany

Date of Birth: March 16, 1969

Educational Institutions Attended:

University of Victoria, Canada	1993 - 1995
Technische Fachhochschule Berlin, Germany	1988 - 1993
Technische Fachoberschule Hamburg, Germany	1986 - 1988

Publications:

Bohlmann, J. and Bradley, C., "A fibre optic interferometer for the measurement of surface topography", COMADEM 95, Kingston, Ont., June 1995.

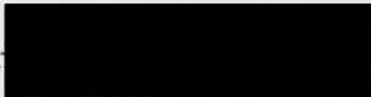
PARTIAL COPYRIGHT LICENSE

I hereby grant the right to lend my thesis to users of the University of Victoria Library, and to make single copies only for such users or in response to a request from the Library of any other university, or similar institution, on its behalf or for one of its users. I further agree that permission for extensive copying of this thesis for scholarly purposes may be granted by me or a member of the University designated by me. It is understood that copying or publication of this thesis for financial gain shall not be allowed without my written permission.

Title of Thesis:

Fibre Optic Sensor for Surface Roughness Measurement

Author


Jan Bohlmann

November 24, 1995